資 料 1

An Experimental Proposal on Nuclear and Particle Physics Experiments at the J-PARC 50 GeV Proton Synchrotron

An Experimental Search for Lepton Flavor Violating $\mu^- - e^-$ Conversion at Sensitivity of 10^{-16} with a Slow-Extracted Bunched Proton Beam

November 30th, 2007

The COMET Collaboration

D. Bryman
Department of Physics and Astronomy, University of British Columbia, Vancouver, Canada

R. Palmer
Department of Physics, Brookhaven National Laboratory, USA

Y. Iwashita
Institute for Chemical Research, Kyoto University, Kyoto, Japan

M. Aoki, Y. Arimoto, Md.I. Hossain, T. Itahashi, Y. Kuno*, A. Sato, M. Yoshida
Department of Physics, Osaka University, Osaka, Japan

Y. Takubo
Department of Physics, Tohoku University, Japan

Y. Igarashi, S. Ishimoto, T. Ogitsu, M. Tomizawa, A. Yamamoto, K. Yoshimura
High Energy Accelerator Research Organization (KEK), Tsukuba, Japan

T. Numao
TRIUMF, Canada

* Contact Person

Abstract

We would like to submit a proposal for a new experiment (COMET) of searching for coherent neutrino-less conversion of a muon to an electron, $\mu^- + N(A,Z) \rightarrow e^- + N(A,Z)$, in muonic atoms ($\mu^- - e^-$ conversion) at a 90 % confidence-level sensitivity of $B(\mu^- N \rightarrow e^- N) < 10^{-16}$. The target sensitivity is a factor of about 10,000 better than the present published limit of $B(\mu^-\mathrm{Au} \rightarrow e^-\mathrm{Au}) < 7 \times 10^{-13}$. This experiment would provide a very large window on new physics beyond the Standard Model.

The experiment is planned to be carry out at the J-PARC Nuclear and Particle Experimental (NP) Hall by using a bunched proton beam that is slow-extracted from the J-PARC main ring, where beam bunching is needed to eliminate beam-related background events and keep an experimental sensitivity as high as possible. The muon beam line considered in this proposed experiment consists of a section of large solid-angle pion capture by surrounding high-field superconducting solenoid magnets, a section of superconducting curved solenoid magnets for transporting muons and selecting their momenta, and a detector section of curved solenoid spectrometer to detect $\mu^- - e^-$ conversion signals with low counting rate environment.

This new initiative has been taken recently to achieve an early and timely start of a series of searches and is regarded as the first step of our staging approach. This would evolve smoothly toward the ultimate search and the discovery of $\mu^- - e^-$ conversion by an experiment with a muon storage ring (PRISM) with a 10^{-18} sensitivity.

Contents

Chapter 1

Physics Motivation

1.1 Introduction

Recently, lepton flavor violation (LFV) of charged leptons[1] has attracted much theoretical and experimental attention, since it has a growing potential to helping in finding important clues for new physics beyond the Standard Model [1]. LFV of charged leptons is one of the flavor changing neutral current (FCNC) processes, where new physics contributions are expected to observe in high precision experiments. Some of the notable features of LFV studies are that (1) LFV of charged leptons could **have sizable contributions from new physics**, which could manifest itself in future experiments, and (2) LFV of charged leptons **does not have any sizable contributions from the Standard Model**, which could become serious background events that would limit sensitivities to new physics, such as in the case for FCNC processes in the quark sector.

Since the first search by Hincks and Pontecorvo in 1947 [2], experimental searches for LFV have been continuously carried out with various elementary particles, such as muons, taus, kaons, and others. The upper limits have been improved at a rate of two orders of magnitude per decade, as can be seen in Fig. 1.1. The present upper limits of various LFV decays are listed in Table 1.1, where it can be seen that the sensitivity of the muon system to LFV is very high. This is mostly because of the large number of muons available for experimental searches nowadays (about $10^{14} - 10^{15}$ muons/year). Moreover, an even greater number of muons (about $10^{19} - 10^{20}$ muons/year) will be available in the future, if new highly intense muon sources are realized.

In the minimal Standard Model, lepton flavor conservation is built in by assuming vanishingly small neutrino masses. However, neutrino mixing has been experimentally confirmed by the discovery of neutrino oscillations, and lepton flavor conservation is known to be violated. However, LFV of charged leptons has yet to be observed experimentally. It is known that the contribution of neutrino mixing to LFV is extremely small, since it is proportional to $(m_\nu/m_W)^4$, yielding the order of 10^{-52} in branching ratios. Therefore, the discovery of LFV would imply new physics beyond

[1]Hereafter, "LFV" is used for lepton flavor violation of charged leptons, even when charged leptons are not explicitly specified.

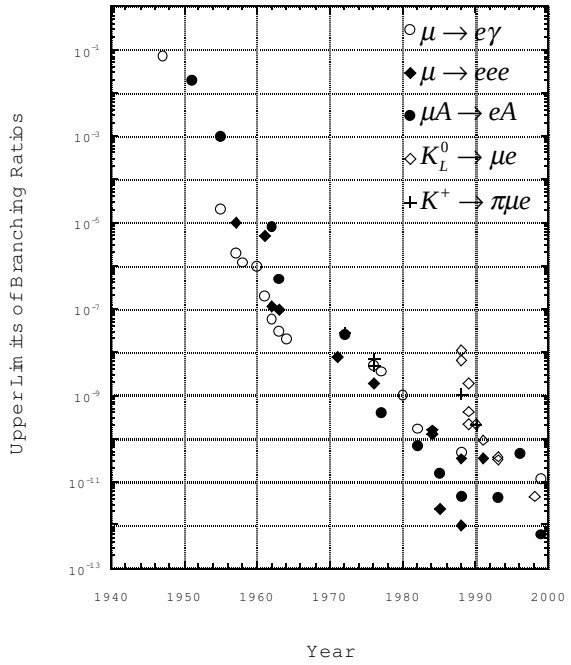

Figure 1.1: History of searches for LFV in muon and kaon decays

Table 1.1: Present limits of LFV of muon, tau, pion, kaon and Z boson.

Reaction	Present limit	Reference
$\mu^+ \to e^+\gamma$	$< 1.2 \times 10^{-11}$	[3]
$\mu^+ \to e^+e^+e^-$	$< 1.0 \times 10^{-12}$	[4]
$\mu^- Ti \to e^- Ti$	$< 6.1 \times 10^{-13}$	[5]
$\mu^- Au \to e^- Au$	$< 7 \times 10^{-13}$	[6]
$\mu^+e^- \to \mu^-e^+$	$< 8.3 \times 10^{-11}$	[7]
$\tau \to e\gamma$	$< 3.9 \times 10^{-7}$	[8]
$\tau \to \mu\gamma$	$< 3.1 \times 10^{-7}$	[9]
$\tau \to \mu\mu\mu$	$< 1.9 \times 10^{-7}$	[10]
$\tau \to eee$	$< 2.0 \times 10^{-7}$	[10]
$\pi^0 \to \mu e$	$< 8.6 \times 10^{-9}$	[11]
$K_L^0 \to \mu e$	$< 4.7 \times 10^{-12}$	[12]
$K^+ \to \pi^+\mu^+e^-$	$< 2.1 \times 10^{-10}$	[13]
$K_L^0 \to \pi^0\mu^+e^-$	$< 3.1 \times 10^{-9}$	[14]
$Z^0 \to \mu e$	$< 1.7 \times 10^{-6}$	[15]
$Z^0 \to \tau e$	$< 9.8 \times 10^{-6}$	[15]
$Z^0 \to \tau\mu$	$< 1.2 \times 10^{-5}$	[16]

"neutrino oscillations". As a matter of fact, any new physics or interactions beyond the Standard Model would predict LFV at some levels. The new physics includes

supersymmetric models, extra dimension models, models with new gauge bosons Z', models with new heavy leptons, lepto-quark models and so on. The motivation for studying the physics of LFV throughout the next decade is very robust. To illustrate, let us consider, as just an example, the case of supersymmetry (SUSY), as follows.

1.2 Supersymmetric Extension

It is known that LFV has significant contributions from SUSY. It is in particular large if SUSY particles exist in the LHC energy range. In minimum SUSY extension (MSSM), LFV of charged leptons would occur through mixing of their corresponding sleptons. Figure 1.2 shows one of the LFV diagrams of SUSY contributing to a muon to electron transition ($\mu \to e+$ "γ"), where the mixing of a smuon ($\tilde{\mu}$) and a selectron ($\tilde{e}$), which is denoted by $\Delta m^2_{\tilde{\mu}\tilde{e}}$ in Fig. 1.2, plays a key role. This slepton mixing parameter, $\Delta m^2_{\tilde{\mu}\tilde{e}}$ (or similarly $\Delta m^2_{\tilde{e}\tilde{\mu}}$) is given by the off-diagonal element of the slepton mass matrix ($m^2_{\tilde{l}}$) that is given in Eq. (1.1).[2]

$$m^2_{\tilde{l}} = \begin{pmatrix} m^2_{\tilde{e}\tilde{e}}, & \Delta m^2_{\tilde{e}\tilde{\mu}}, & \Delta m^2_{\tilde{e}\tilde{\tau}} \\ \Delta m^2_{\tilde{\mu}\tilde{e}}, & m^2_{\tilde{\mu}\tilde{\mu}}, & \Delta m^2_{\tilde{\mu}\tilde{\tau}} \\ \Delta m^2_{\tilde{\tau}\tilde{e}}, & \Delta m^2_{\tilde{\tau}\tilde{\mu}}, & m^2_{\tilde{\tau}\tilde{\tau}} \end{pmatrix} \tag{1.1}$$

Therefore, the determination of these SUSY contributions would enable us to study the structure of the slepton mass matrix, and then more importantly "SUSY soft breaking" that is the origin of SUSY particle masses. It should be noted that the slepton mixing is difficult to study, as precisely as in LFV studies, at high energy collider experiments such as the LHC. Hence, studies of LFV would provide a **unique opportunity to study the slepton mixing**. In the following, the SUSY contributions to LFV are presented in more details.

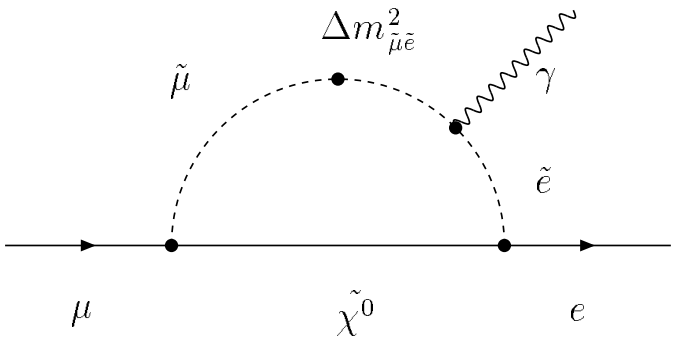

Figure 1.2: One of the diagrams of SUSY contributions to a μ to e transition ($\mu \to e+$ "γ"). $\Delta m^2_{\tilde{\mu}\tilde{e}}$ indicates the magnitude of the slepton mixing.

[2]It is note-worthy that the SUSY contributions to the muon $g-2$ and the muon EDM are a real and an imaginary parts of the diagonal element of $m^2_{\tilde{\mu}\tilde{\mu}}$, respectively.

1.2.1 mSUGRA Models

There are three different scenarios for SUSY soft breaking. One of them is gravity mediated soft breaking, which is called supergravity (SUGRA) models. In minimum SUGRA models (mSUGRA), the slepton mass matrix is assumed to be diagonal at the Planck mass scale ($\sim 10^{19}$ GeV), and no off-diagonal matrix elements exits ($\Delta m^2_{\tilde{\mu}\tilde{e}} = 0$). Then, non-zero off-diagonal matrix elements can be induced by radiative corrections from the Planck scale to the weak scale ($\sim 10^2$ GeV).

There could be two potential sources s at high energy to induce off-diagonal elements of the slepton mass matrix, as shown in Fig. 1.3. One of the sources is grand unification (GUT) at $\sim 10^{16}$ GeV, where the GUT Yukawa interaction creates non-zero off-diagonal elements. This scenario is called a **SUSY-GUT** model. And the other source is the neutrino seesaw mechanism, where the neutrino Yukawa interaction does. This scenario is called a **SUSY-Seesaw** model.

Both models predict large branching ratios for LFV, which are just a few orders of magnitude below the current experimental upper limits. Therefore, if we could improve experimental sensitivity by a few orders of magnitude, this would provide a great potential for new discoveries.

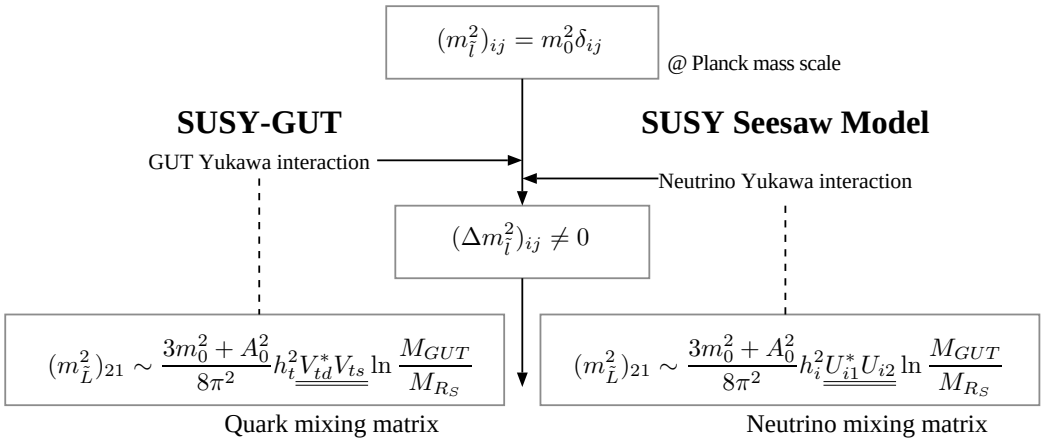

Figure 1.3: Two physics mechanisms (SUSY-GUT and SUSY-Seesaw) would introduce non-zero off-diagonal matrix elements, leading the slepton mixing, in the mSUGRA model.

1.2.1.1 Predictions of SUSY-GUT Models

In SUSY-GUT, the non-zero slepton mixing appears unavoidably through radiative corrections in the renormalization group evolution from the GUT scale to the weak energy scale [17]. It is given by

$$\Delta m^2_{\tilde{\mu}\tilde{e}} \propto \frac{3m_0^2 + A_0^2}{8\pi^2} h_t^2 V^*_{td} V_{ts} \ln \frac{M_{GUT}}{M_{R_3}} \tag{1.2}$$

where m_0 is the universal scalar mass. V_{td} and V_{ts} are the Kobayashi-Maskawa (KM) quark mixing matrix elements. Recently, it was pointed out that the slepton mixing thus generated could be very large owing to the large top-quark Yukawa coupling [18]. The branching ratios of $\mu^- - e^-$ conversion predicted in SUSY SU(5) models [1] are shown in Fig. 1.4. They range from 10^{-15} to 10^{-13} for the singlet smuon mass of $m_{\tilde{\mu}_R}$ of 100 to 300 GeV [19]. They are larger for a large $\tan\beta$ value. The SO(10) SUSY GUT models give an even larger value of 10^{-13} to 10^{-11} by an enhancement of $(m_\tau^2/m_\mu^2) \sim 100$ [18]. It is because of the existence of loop diagrams whose magnitude is proportional to the tau-lepton mass in SO(10) SUSY-GUT models.

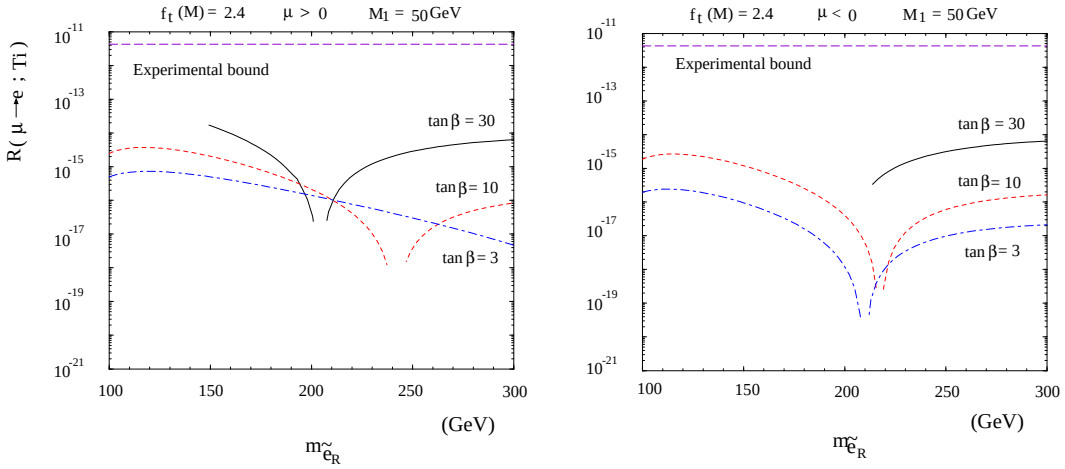

Figure 1.4: Predicted branching ratios for $\mu^- - e^-$ conversion in SUSY-GUT. μ is one of the SUSY parameters, and $\mu > 0$ (left) and $\mu < 0$ (right).

1.2.1.2 Predictions of SUSY-Seesaw Models

The other model is the supersymmetric model with the neutrino seesaw mechanism, which predict the existence of right-handed heavy neutrinos, ν_R. As widely known, there is experimental evidence for the existence of neutrino masses and their mixing. In the SUSY model with the seesaw mechanism, the slepton mixing can be induced from the neutrino mixing. Then, LFV processes in muon decays are also expected to occur [20, 21, 22]. In principle, there can be potentially two contributions to the slepton mixing $\Delta m^2_{\tilde{\mu}\tilde{e}}$. One is from $U_{\mu e}$ corresponding to the solar neutrino mixing. The other is from the product of $U_{\tau e}$ and $U_{\tau\mu}$ that corresponds to the atmospheric neutrino mixing. Assuming the tau Yukawa coupling is large, the second contribution can be large. In this case, the slepton mixing can be given by

$$\Delta m^2_{\tilde{\mu}\tilde{e}} \propto \frac{3m_0^2 + A_0^2}{8\pi^2} h_\tau^2 U^*_{\tau e} U_{\tau\mu} \ln \frac{M_{GUT}}{M_{R_3}} \tag{1.3}$$

where $U_{\tau e}$ and $U_{\tau\mu}$ are the Maki-Nakagawa-Sakata (MNS) neutrino mixing matrix elements. h_τ is the tau Yukawa coupling. The prediction is shown in Fig.1.2.1.2.

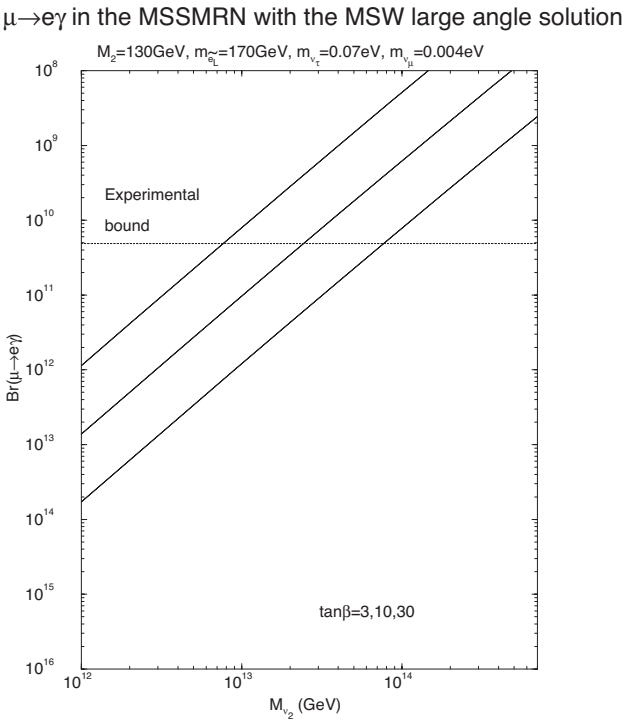

Figure 1.5: Predictions of $\mu^+ \to e^+\gamma$ branching ratio in SUSY-Seesaw models. The three lines correspond to the cases of $\tan\beta = 30, 10, 3$ from top to bottom, respectively.

These two possible mechanisms to make slepton mixing in MSSM (supergravity SUSY) is shown in Fig. 1.3. In SUSY-GUT cases, the slepton mixing is given by the product of the KM matrix elements, while in SUSY-Seesaw cases, it is given by the product of the MNS matrix elements.

1.2.2 Gauge Mediated SUSY Breaking Models

Another type of SUSY breaking is the Gauge mediated SUSY breaking models. In these models, flavor violation of quarks and leptons is highly suppressed. And thereby LFV is too small to be observed in principle. However, when the neutrino seesaw mechanism is included in SUSY models and the right-handed neutrinos are lighter than the messenger scale of gauge mediation, sizable LFV effects of charged leptons are expected [23]. The predictions of this model is presented in Fig. 1.6.

1.3 LFV and High-energy Frontier

In this section, the relations between the search for LFV and high-energy frontier is described, in particular in terms of SUSY models. There are two possible cases, namely the case when the LHC finds SUSY, and the other case when the LHC cannot find SUSY.

When the LHC finds SUSY, charged lepton mixing attract more interest, because the LHC (nor the ILC) **cannot study the slepton mixing as precisely as in the LFV studies**. LFV studies would become more important in terms of examining either SUSY-GUT or SUSY-Seesaw models, through slepton mixing.

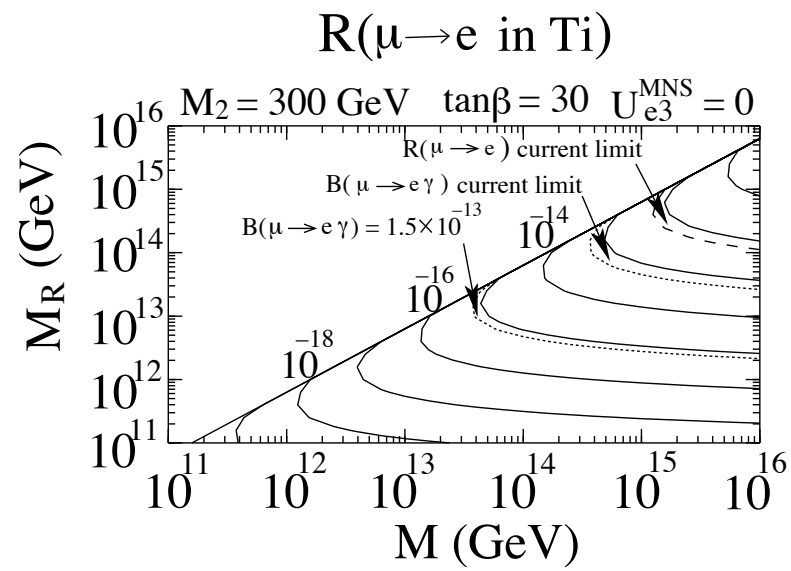

Figure 1.6: Predictions of the gauge mediated supersymmetric breaking models. When the neutrino seesaw mechanism is included in this type of SUSY models and the right-handed neutrinos are lighter than the messenger scale of gauge mediation, large LFV of charged leptons are expected.

If LHC cannot find evidence for SUSY, two cases can be considered; either SUSY does not exist at all or SUSY only exists for heavier masses on a multiple TeV scale. High-precision measurements with intense slow muons become very important, since such measurements are sensitive to a heavier mass scale than what can be reached by high-energy accelerators.

For heavier SUSY, if the LFV search has a sufficient experimental sensitivity (such as 10^{-18} for $\mu^- - e^-$ conversion), it could reach the SUSY mass scale up to several TeV that the LHC cannot reach for particular SUSY parameter cases. One of examples is shown in Fig.1.7, which is a sensitivity plot for the SUSY parameters of one of the mSUGRA bench mark point, called "Focus Point" with $\mu < 0$ [24]. The red lines are theoretical predictions for various $\sin\theta_{13}$ values. Therefore, the search for LFV would be worth carrying out even if the LHC does not find evidence for SUSY below the TeV energy scale.

It should be noted that besides SUSY, there are other models that predict sizable effects of LFV. These include heavy neutrino models, leptoquark models, composite models, two Higgs doublet models, second Z' models, and anomalous Z coupling.

In summary, the LFV search is very robust in physics motivation, even in the LHC era.

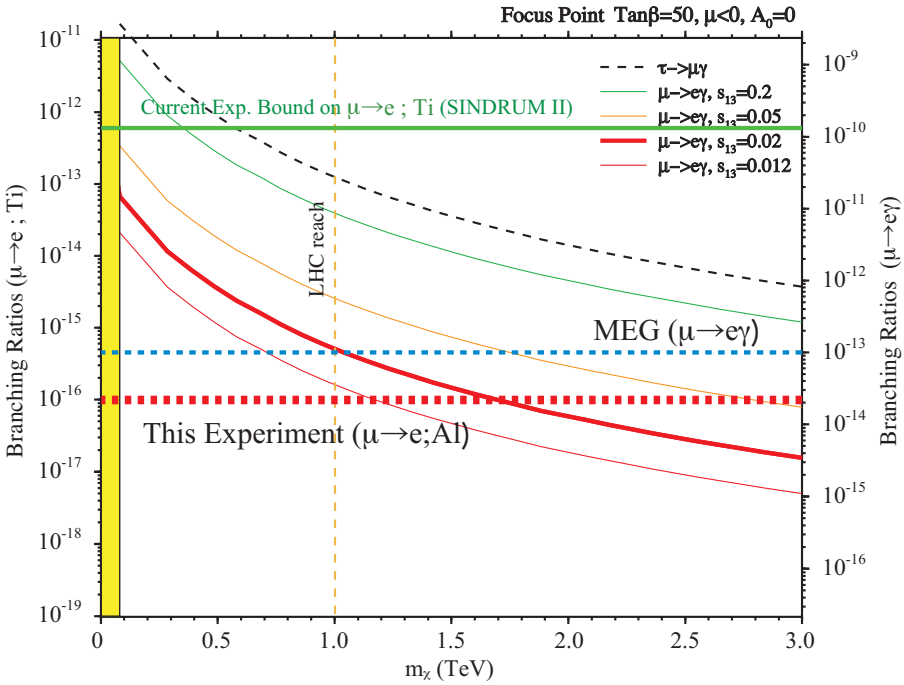

Figure 1.7: Prediction of the branching ratio of $\mu^- - e^-$ conversion in Ti in the SUSY-Seesaw models as a function of SUSY mass scale (neutralino). The sensitivity of the proposed experiment is also shown.

Chapter 2

Phenomenology of $\mu^- - e^-$ Conversion

2.1 What is a $\mu^- - e^-$ Conversion Process ?

One of the most prominent muon LFV processes is coherent neutrino-less conversion of muons to electrons ($\mu^- - e^-$ conversion), $\mu^- + N(A,Z) \rightarrow e^- + N(A,Z)$. When a negative muon is stopped by some material, it is trapped by an atom, and a muonic atom is formed. After it cascades down energy levels in the muonic atom, the muon is bound in its $1s$ ground state. The fate of the muon is then to either decay in orbit ($\mu^- \rightarrow e^- \nu_\mu \overline{\nu}_e$) or be captured by a nucleus of mass number A and atomic number Z, namely, $\mu^- + (A,Z) \rightarrow \nu_\mu + (A, Z-1)$. However, in the context of physics beyond the Standard Model, the exotic process of neutrino-less muon capture, such as

$$\mu^- + (A,Z) \rightarrow e^- + (A,Z), \tag{2.1}$$

is also expected. This process is called $\mu^- - e^-$ conversion in a muonic atom. This process violates the conservation of lepton flavor numbers, L_e and L_μ, by one unit, but the total lepton number, L, is conserved. The final state of the nucleus (A,Z) could be either the ground state or one of the excited states. In general, the transition to the ground state, which is called coherent capture, is dominant. The rate of the coherent capture over non-coherent capture is enhanced by a factor approximately equal to the number of nucleons in the nucleus, since all of the nucleons participate in the process.

2.2 Signal and Background Events

The event signature of coherent $\mu^- - e^-$ conversion in a muonic atom is a mono-energetic single electron emitted from the conversion with an energy of $E_{\mu e} \sim m_\mu - B_\mu$, where m_μ is the muon mass, and B_μ is the binding energy of the $1s$ muonic atom.

From an experimental point of view, $\mu^- - e^-$ conversion is a very attractive process. Firstly, the e^- energy of about 105 MeV is far above the end-point energy of the muon decay spectrum ($\sim$ 52.8 MeV). Secondly, since the event signature is a mono-energetic

electron, no coincidence measurement is required. The search for this process has the potential to improve sensitivity by using a high muon rate without suffering from accidental background events, which would be serious for other processes, such as $\mu^+ \to e^+\gamma$ and $\mu^+ \to e^+e^+e^-$ decays.

The electron is emitted with an energy $E_e \approx m_\mu$, which coincides with the end-point of muon decay in orbit (DIO), which is the only relevant intrinsic physics background event. Since the energy distribution of DIO falls steeply above $m_\mu/2$, the experimental setup may have a large signal acceptance and the detectors can still be protected against the vast majority of decay and capture background events. Energy distributions for DIO electrons have been calculated for a number of muonic atoms [25, 26] and energy resolutions of the order of 0.1% are sufficient to keep this background below 10^{-18}.

There are several other potential sources of electron background events in the energy region around 100 MeV, involving either beam particles or cosmic rays. Beam-related background events may originate from muons, pions or electrons in the beam. Apart from DIO, muons may produce background events by muon decay in flight or radiative muon capture (RMC). Pions may produce background events by radiative pion capture (RPC). Gamma rays from RMC and RPC produce electrons mostly through e^+e^- pair production inside the target.

There are three methods to suppress the beam-related background events:

- Beam pulsing
  Since muonic atoms have lifetimes of the order of 1 μs, a pulsed beam with buckets that are short compared with this lifetime would allow one to remove prompt background events by performing measurements in a delayed time window. As will be discussed below there are stringent requirements on beam extinction during the measuring interval.
- Beam purity
  Lifetime of pion (26 ns)is much shorter than the lifetime of muon (2200 ns). Thus, if the beam momentum is low enough, most of beam pions will decay away as they transport through a muon beamline. If the beam momentum is less than 70 MeV/c, a level of pion contamination will be decreased by an order of magnitudes for each 10 m.
- Beam Momentum
  In-flight decay of beam muons would produce 100 MeV/c electrons if the beam momentum is larger than 70 MeV/c. Beam electron would be also a source of 100 MeV/c electron background if they are scattered off. Thus, if the beam momentum is restricted to be lower than 70 MeV/c, those background could be suppressed. Lowering the beam momentum is very important.

2.3 $\mu^- - e^-$ conversion vs. $\mu^+ \to e^+\gamma$

There are considered to be two possible contributions in the $\mu^- - e^-$ transition diagrams. One is a photonic contribution, and the other is a non-photonic contribution.

For the photonic contribution, there is a definite relation between the $\mu^- - e^-$ conversion process and the $\mu^+ \to e^+\gamma$ decay. Suppose the photonic contribution is dominant, the branching ratio of the $\mu^- - e^-$ conversion process is expected be smaller than that of $\mu^- - e^-$ decay by a factor of fine structure constant α (a few hundred). This implies that the search for $\mu^- - e^-$ conversion at the level of 10^{-16} is comparable to that for $\mu^+ \to e^+\gamma$ at the level of 10^{-14}.

If the non-photonic contribution dominates, the $\mu^+ \to e^+\gamma$ decay would be small whereas the $\mu^- - e^-$ conversion could be sufficiently large to be observed. It is worth noting the following. If a $\mu^+ \to e^+\gamma$ signal is found, the $\mu^- - e^-$ conversion signal should also be found. A ratio of the branching ratios between $\mu^+ \to e^+\gamma$ and $\mu^- - e^-$ carries important information of the physics process behind. If no $\mu^+ \to e^+\gamma$ signal is found, there will still be an opportunity to find a $\mu^- - e^-$ conversion signal because of the potential existence of non-photonic contributions.

2.4 Present Experimental Status

2.4.1 $\mu^- - e^-$ Conversion

Table 2.1 summarizes the history of searches for $\mu^- - e^-$ conversion. From Table 2.1, it is seen that for about 30 years the experimental upper limits has been improved by 6 orders of magnitude. In the following, the past and future experiments of searching for $\mu^- - e^-$ conversion will be described.

Table 2.1: Past experiments on $\mu^- - e^-$ conversion. (* reported only in conference proceedings.)

Process	upper limit	place	year	reference
$\mu^- + Cu \to e^- + Cu$	$< 1.6 \times 10^{-8}$	SREL	1972	[27]
$\mu^- + {}^{32}S \to e^- + {}^{32}S$	$< 7 \times 10^{-11}$	SIN	1982	[28]
$\mu^- + Ti \to e^- + Ti$	$< 1.6 \times 10^{-11}$	TRIUMF	1985	[29]
$\mu^- + Ti \to e^- + Ti$	$< 4.6 \times 10^{-12}$	TRIUMF	1988	[30]
$\mu^- + Pb \to e^- + Pb$	$< 4.9 \times 10^{-10}$	TRIUMF	1988	[30]
$\mu^- + Ti \to e^- + Ti$	$< 4.3 \times 10^{-12}$	PSI	1993	[31]
$\mu^- + Pb \to e^- + Pb$	$< 4.6 \times 10^{-11}$	PSI	1996	[32]
$\mu^- + Ti \to e^- + Ti$	$< 6.1 \times 10^{-13}$	PSI	1998*	[5]
$\mu^- + Au \to e^- + Au$	$< 7 \times 10^{-13}$	PSI	2006	[6]

2.4.1.1 SINDRUM-II

The latest search for $\mu - e$ conversion was performed by the SINDRUM II collaboration at PSI. Figure 2.1 shows their results. The main spectrum, taken at 53 MeV/c, shows the steeply falling distribution expected from muon DIO. Two events were found at

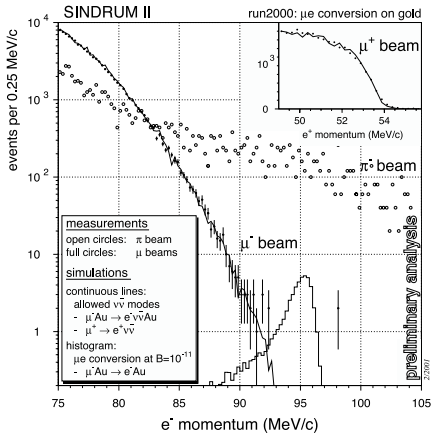

Figure 2.1: Recent results by SINDRUM II. Momentum distributions for three different beam momenta and polarities: (i) 53 MeV/c negative, optimized for μ^- stops, (ii) 63 MeV/c negative, optimized for π^- stops, and (iii) 48 MeV/c positive, optimized for μ^+ stops. The 63 MeV/c data were scaled to the different measuring times. The μ^+ data were taken using a reduced spectrometer field.

higher momenta, but just outside the region of interest. The agreement between measured and simulated positron distributions from μ^+ decay means that confidence can be high in the accuracy of the momentum calibration. At present there are no hints concerning the nature of the two high-momentum events: they might have been induced by cosmic rays or RPC, for example. They set the current upper limit on $B(\mu^- + \mathrm{Au} \to e^- + \mathrm{Au}) < 7 \times 10^{-13}$ [6].

2.4.1.2 MECO

There was an experimental proposal at BNL, which was called the MECO experiment [33], aiming to search with a sensitivity of 10^{-16}. This project was planned to combat beam-related background events with the help of a pulsed 8 GeV/c proton beam. Fig-

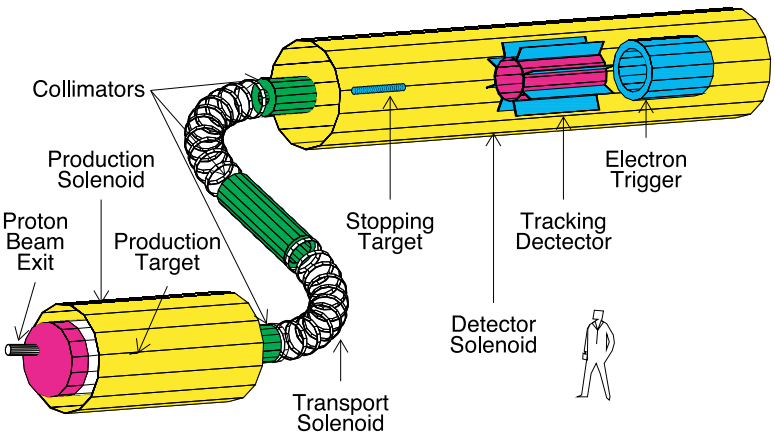

Figure 2.2: Setup of the MECO experiment.

ure 2.2 shows the proposed layout. Pions are produced by 8 GeV/c protons crossing a 16 cm long tungsten target, and muons from the decays of the pions are collected efficiently with the help of a graded magnetic field. Negatively charged particles with 60–120 MeV/c momenta are transported by a curved solenoid to the experimental target. In the spectrometer magnet, a graded field is also applied. A major challenge is the requirement for proton extinction in between the proton bursts. In order to maintain the pion stop rate in the 'silent' interval, a beam extinction factor better than 10^{-8}–10^{-9} is required. Unfortunately, the MECO experiment was canceled in 2005, owing to the NSF funding problems.

2.4.1.3 Mu2e

However, the revival of the MECO experiment has been actively made at the Fermi National Laboratory (Fermilab) by ex-members from the MECO experiment. It is called the "Mu2e experiment". The muon beam line and detector for the Mu2e experiment are exactly the same as those of the MECO experiment. The aimed experimental sensitivity is the same as well. The Expression of Interest (EoI) was presented early spring, 2007 and the Letter of Intent (LoI) has been submitted to the Fermilab PAC, September, 2007 [39]. The Mu2e experiment would strongly compete with us (the COMET experiment)

The Mu2e experiment will be implemented to Fermilab proton source, and the desired proton beam structure from their 8 GeV Booster can be made by reusing the 8 GeV Debuncher and Accumulator storage rings, which are both housed in the anti-proton beam enclosure. At this moment, anti-protons from the production target are transported into the Debuncher ring where they are phase-rotated and stochastically cooled, and then are transferred into the Accumulator ring, where they are momentum stacked. For the Mu2e experiment, proton bunches from the Fermilab Booster are transported through the Recycler ring and injected directly into the Accumulator ring, where they are momentum-stacked. Then, they are transferred into the Debuncher ring and rebunched into a single short bunch. Finally the beam would be resonantly

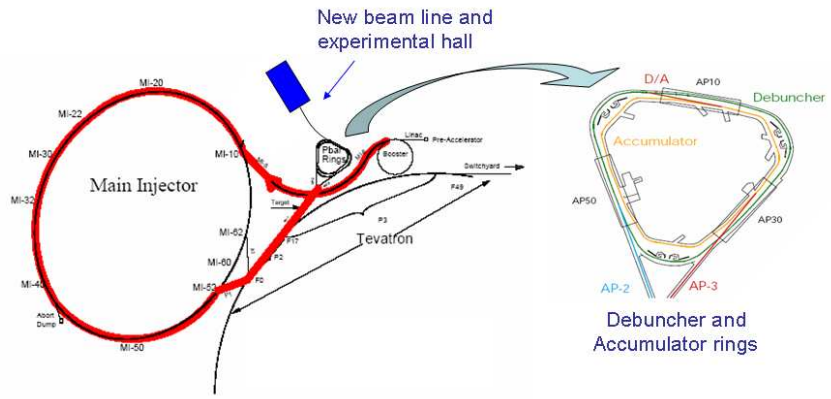

Figure 2.3: Fermilab proton accelerator complex relevant to the Mu2e experiment.

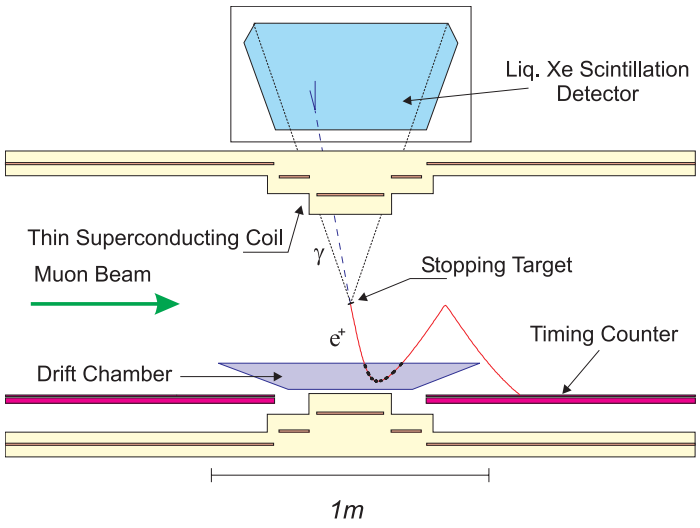

Figure 2.4: Setup of the MEG experiment.

extracted in a such way that the single bunch would cause a bunch train. The proton accelerator complex at Fermilab relevant to the Mu2e experiment is shown in Fig. 2.3.

There are several scenarios on proton delivery for the Mu2e experiment. In the period of the NOνA program after the Tevatron shutdown, the Mu2e would receive about 4×10^{20} protons for several years, with the upgrades of the Booster repetition and improvement of the beam transmission efficiency of the Booster. In Fermilab, there are proton upgrade plans, such as the "SuperNuMI" (SNuMI) plan, where the beam power to the NuMI beam line to roughly 1.2 MW, and more ambitiously the "Project-X" plan, where a new 8 GeV linac with superconducting RFs would increase to 2 MW (3×10^{21} protons/sec). In the both cases, protons delivered from the Fermilab proton sources would increase.

2.4.2 $\mu^+ \to e^+\gamma$ Decay

The present experimental limit for $\mu^+ \to e^+\gamma$ is 1.2×10^{-11}, which was obtained by the MEGA experiment at LANL in the US [3].

A new experiment called MEG at PSI [34], which aims to achieve a sensitivity of 10^{-13} in the $\mu^+ \to e^+\gamma$ branching ratio, is under construction. A schematic view of the detector is shown in Fig. 2.4. The improved experiment will be expected to utilize a continuous muon beam of 100% duty factor at PSI. Utilizing the same instantaneous beam intensity as MEGA, the total number of muons available can be increased by a factor of 16. A further improvement is the use of a novel liquid xenon scintillation detector of the "Mini-Kamiokande" type, which is a 0.8-m^3 volume of liquid xenon observed by an array of 800 photomultipliers from all sides. For e^+ detection, a solenoidal magnetic spectrometer with a graded magnetic field is to be adopted. The engineering run has been started in the year 2007, and physics data taking is expected to start soon.

2.5 Why is $\mu^- - e^-$ Conversion the Next Step ?

Considering its marked importance to physics, it is highly desirable to consider a next-generation experiment to search for LFV. There are three processes to be considered; namely, $\mu^+ \to e^+\gamma$, $\mu^+ \to e^+e^+e^-$, and $\mu^- - e^-$ conversion.

The three processes have different experimental issues that need to be solved to realize improved experimental sensitivities. They are summarized in Table 2.2. The processes of $\mu^+ \to e^+\gamma$ and $\mu^+ \to e^+e^+e^-$ are detector-limited. To consider and go beyond the present sensitivities, the resolutions of detection have to be improved, which is, in general, very hard. In particular, improving the photon energy resolution is difficult. On the other hand, for $\mu^- - e^-$ conversion, there are no accidental background events, and an experiment with higher rates can be performed. If a new muon source with a higher beam intensity and better beam quality for suppressing beam-associated background events can be constructed, measurements of higher sensitivity can be performed.

Table 2.2: LFV processes and issues

Process	Major backgrounds	Beam	Sensitivity Issues
$\mu^+ \to e^+\gamma$	accidental	DC beam	detector resolution
$\mu^+ \to e^+e^+e^-$	accidental	DC beam	detector resolution
$\mu^- - e^-$ conversion	beam-associated	pulsed beam	beam qualities

Furthermore, it is known that in comparison with $\mu^+ \to e^+\gamma$, there are more physical processes that $\mu^- - e^-$ conversion and $\mu^+ \to e^+e^+e^-$ could contribute to. Namely, in SUSY models, photon-mediated diagrams can contribute to all the three processes, but the Higgs-mediated diagrams can contribute to only $\mu^- - e^-$ conversion and $\mu^+ \to e^+e^+e^-$. In summary, with all of the above considerations, a search for $\mu^- - e^-$ conversion would be the natural next step to take to realize an improved experiment.

Chapter 3

Overview of the Experiment

3.1 Overview

We would like to submit a new proposal to carry out a new experiment of searching for coherent neutrino-less conversion of muons to electron in a muonic atom ($\mu^- - e^-$ conversion), $\mu^- + N(A,Z) \rightarrow e^- + N(A,Z)$, at a sensitivity of 10^{-16}, at the Japanese Proton Accelerator Research Complex (J-PARC). The aimed sensitivity is **a factor of 10,000 better** than that of current experimental limit[1].

The experiment is proposed to carry out in the J-PARC Nuclear and Particle Experimental Hall (NP Hall) by using a bunched proton beam slow-extracted from the J-PARC MR. An experimental setup consists of high-field pion capture solenoids, curved solenoids to select beam momenta, and a curved solenoid spectrometer to detect $\mu^- - e^-$ conversion with low-counting-rate conditions. A schematic drawing of the experimental setup is shown in Fig. 3.1.

To improve the sensitivity by a factor 10,000 over the current limit, several important features have been considered, as highlighted below.

- **Highly Intense Muon Source**: To achieve an experimental sensitivity of 10^{-16}, the total number of muons needed is of the order of 10^{18}. Therefore, a highly intense muon beam line has to be constructed. To increase the muon beam intensity, two methods are adopted in this experiment. One is to use a proton beam of high beam power. The other is to use a system of collecting pions, which are parents of muons, with high efficiency. In the muon collider and neutrino factory R&D, *superconducting solenoid magnets* producing a high magnetic field surrounding the proton target have been proposed and studied for pion capture over a large solid angle. With the pion capture solenoid system, about 8×10^{20} protons of 8 GeV are necessary to achieve the number of muons of the order of 10^{18}.

- **Pulsed Proton Beam**: There are several potential sources of electron background events in the energy region around 100 MeV, where the $\mu^- - e^-$ conver-

[1] The present published limit is $B(\mu^- + \mathrm{Au} \rightarrow e^- + \mathrm{Au}) = 7 \times 10^{-13}$ from SINDRUM-II at PSI [6].

sion signal is expected. One of them is beam-related background events. To suppress the occurrence of beam-related background events, a pulsed proton beam utilizing "*beam pulsing*" is proposed. Since muons in muonic atoms have lifetimes of the order of 1 μsec, a pulsed beam with beam buckets that are short compared with these lifetimes would allow removal of prompt beam background events by allowing measurements to be performed in a delayed time window. As will be discussed below, there are stringent requirements on the *beam extinction* during the measuring interval. Tuning of a proton beam in the accelerator ring as well as extra extinction devices should be installed to achieve the required level of beam extinction.

- **Muon Transport System with Curved Solenoids**: The captured pions decay to muons, which are transported with high efficiency through a superconducting solenoid magnet system. Beam particles with high momenta would produce electron background events in the energy region of 100 MeV, and, therefore, they must be eliminated with the use of curved solenoids where the centers of the helical motion of the electrons drift perpendicular to the plane in which their paths are curved, and the magnitude of the drift is proportional to their momentum. By using this effect and by placing suitable collimators at appropriate locations, beam particles of high momenta can be eliminated.

- **Spectrometer with Curved Solenoids**: To reject electron background events and reduce the probability of false-tracking owing to high counting rates, a curved solenoid spectrometer is considered to allow selection of electrons on the basis of their momenta. The principle of momentum selection is the same as that used in the transport system, but, in the spectrometer, electrons of low momenta which mostly come from muon decay in orbit (DIO) are removed. The detection rate of DIO electrons would be about 1000 tracks per second (1000 Hz), whereas the MECO experiment expected hit rates of about 500 kHz per single wire of the tracking device.

3.2 Prospects and Future Extension to PRISM

We are working on another ambitious project of aiming at a sensitivity of 10^{-18} with a muon storage ring and a fast-extracted proton beam. It is called "PRISM". Letters of Intent (LoI) on PRISM have been submitted in the past J-PARC PAC [35, 36, 37]. As discussed in those LoIs, PRISM might require a new experimental facility with a new fast-extracted proton beam line at the J-PARC MR. The construction of a new experimental facility would require major civil construction, and might take a substantial amount of budget and time. And also to realize PRISM, major R&D efforts is needed as well. From these, it is not possible to realize PRISM soon.

On the other hand, physics motivation and urgency of searching for $\mu^- - e^-$ conversion is very high. As described before, in the U.S., a new experimental program called "mu2e" has been established at the Fermi National Laboratory (Fermilab),

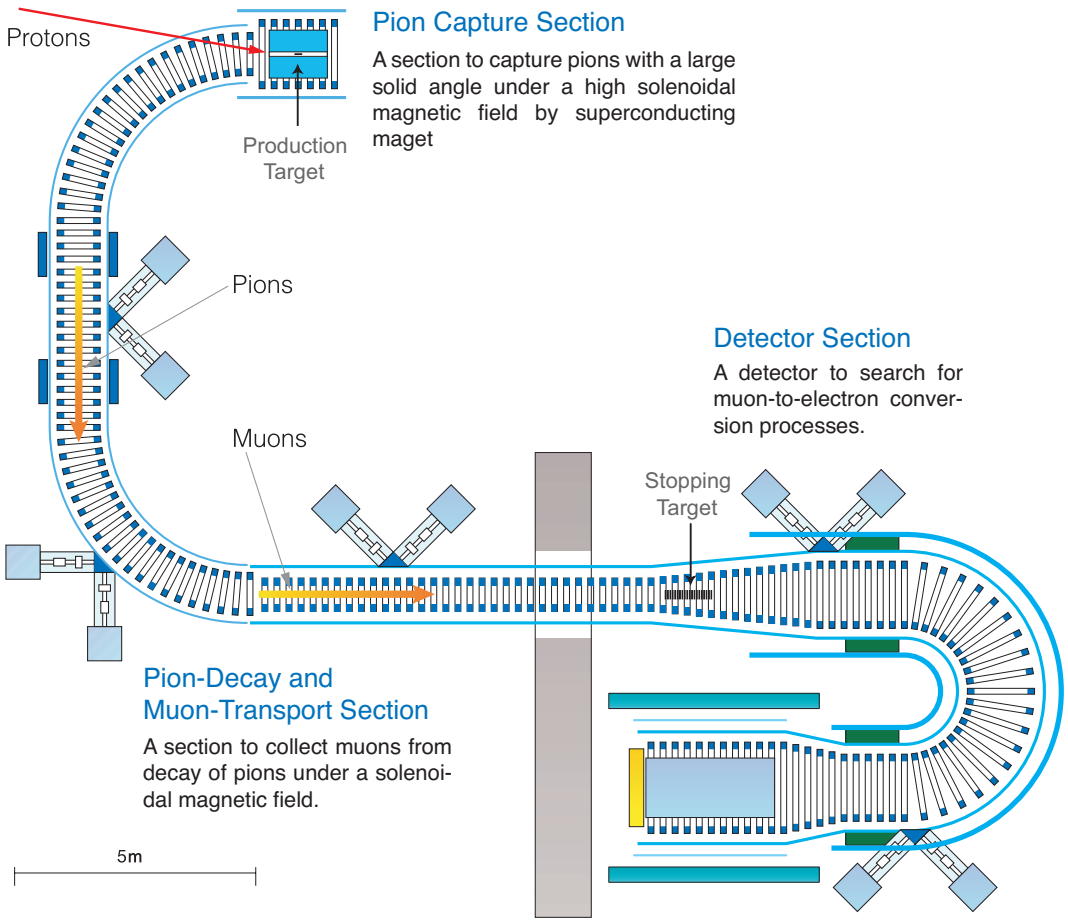

Figure 3.1: Schematic layout of the muon beamline and detector for the proposed search for $\mu^- - e^-$ conversion, the COMET experiment.

as a revival of the MECO experiment. They are evolving quickly to carry out it at Fermilab. Therefore, the competition is very severe. We believe that the proposed experiment, COMET, is a better experiment than the mu2e experiment. It is very critical to launch the proposed COMET experiment as soon as possible.

This new initiative aiming at 10^{-16} with a bunched proton beam with slow extraction has been taken to achieve an early start and also to compete with the mu2e experiment at Fermilab. The COMET experiment is regarded as the first step of a series of searches for $\mu^- - e^-$ conversion. After this experiment, further improvements will be sought at a sensitivity of 10^{-18} with the development of PRISM, by adding a muon storage ring.

Chapter 4

The Muon Source

In this chapter, a new highly-intense muon source that is designed for this experiment is described. The J-PARC main ring (MR) is used to supply a pulsed 8 GeV proton beam. It is extracted using slow extraction with keeping its bunch structure into the J-PARC Nuclear and Particle Experimental Hall (NP Hall). The pulsed proton beam hit a pion production target, which is located inside of the pion capture solenoid magnet. Low energy pions emerging out of the production target are captured by a solenoidal magnetic field. The pions are transported along the magnetic field down to the muon transport section, which is composed of long straight and curved solenoid magnets, where pions decay to muons. Then, the muons are momentum selected using curved solenoid magnetic fields.

4.1 Pulsed Proton Beam

The J-PARC MR would deliver a proton beam of its intensity of 3.3×10^{14} protons per cycle with its cycle time of about 0.3 Hz. Protons from the J-PARC MR are extracted either to the NP Hall by slow extraction, or to the neutrino experimental hall (T2K) by fast extraction. When operated in the slow extraction mode, an average beam current and a duty factor are 15 μA and 0.2 respectively.

This experiment will be constructed at the J-PARC NP Hall, because the proposed experiment needs a bunched proton beam from slow extraction. At J-PARC, the NP Hall is the only experimental hall that has a slow-extracted proton beam. The proton beam from J-PARC MR will have an energy of up to 30 GeV (maximum) and a beam current of about 15μA (maximum).[1], yielding proton beam power of about 450 kW, which is the strongest worldwide among GeV proton machines.

4.1.1 Beam Requirements

In this section, the requirements for the proton beam and a potential scheme to meet those requirements are described.

[1]In the initial stage, because beam energy at the proton linear accelerator (LINAC) is lower, the beam current is expected to be about 9 μA.

4.1.1.1 Proton beam current

Achieving a high sensitivity in searches for rare processes requires a high flux of a beam. To realize the target sensitivity of 10^{-16} in the branching ratio of $\mu^- - e^-$ conversion, about 10^{18} muons in total are required, as will be discussed in Chapter 6. On the basis of the current design of the muon beam line, about 16×10^{20} protons with an energy of 8 GeV are needed. Assuming a beam intensity of 4×10^{13} protons per second (which corresponds to a beam current of about 7 μA), a running time of about 4×10^7 sec, which corresponds to about 16 months, is needed.[2]

4.1.1.2 Proton energy

A number of pions (and therefore their daughter, muons) produced by a proton beam is proportional to proton beam power which is given by the product of its beam energy and its beam current. Roughly speaking, as long as the beam power is the same, the pion yield would be almost the same. It is based on the fact that the pion cross section increases linearly as proton beam energy. This requirement of beam power is about the same as that in the MECO experiment at BNL-AGS [38] and the Mu2e experiment at Fermilab [39].

It is noted that the reason why a low proton beam energy like 8 GeV is considered is two-fold. One is to suppress production of anti-protons, as will be discussed in Chapter 6, and the other is related to beam extinction, where a lower beam energy is easier to kick off, as described in Section 4.1.2.4.

4.1.1.3 Proton beam emittance

The beam emittance should be less than the acceptance of a hadron beam line. Although the hadron beam line acceptance is 30π mm·mrad, the core emittance of the beam has to be controlled much less than that, namely about 10π mm·mrad for both vertical and horizontal. Otherwise, the radiation coming from the beam loss would become serious problem.

4.1.1.4 Proton bunch structure

The time structure of the proton beam has to be pulsed, and the time separation of the pulses should be about 1 μsec. The signal electron will be emitted with a negative muon lifetime in a target (about 1 μsec), thus it will enter the detector during an interval between the proton pulses. On the other hand, the beam related background will come at the proton pulse timing since these are mostly prompt timing processes. This timing information is very important measurement to distinguish signals and backgrounds. If there is a residual protons between the proton pulses, it will produce the beam related background in the signal timing. In order to prevent this, the

[2]The required running time depends on the materials of the pion production target. The current choice is graphite. But, if tungsten is used, the pion production yield increase by a factor of two, and therefore 8×10^{20} protons, generated by 7 μA with a running time of 2×10^7 sec, would be sufficient. Technical issues to use tungsten will be studied.

residual protons in between the pulses should be reduced to 10^{-9} or less than that. We call this a beam *extinction*.

The number of protons in a pulse should be controlled to be less than a limit given by the detector performance. In our design, the detector has an excellent capability of eliminating the low energy charged particles as well as neutral particles. According to the Monte Carlo estimation, the amount of the charged particle tracks entering to the sensitive detector is $10^{-8} \sim 10^{-7}$ of those emerging out of the muon stopping target. Thus, if we want to limit the number of tracks hitting the sensitive detector in a μsec being less than 10 tracks, the number of protons in a pulse should be 10^{11} or less. This means the number of pulses per cycle should be an order of 100 or more.

On the other hand, it is quite helpful to reduce the total live time of the detector for suppressing the cosmic-ray background. From that point of view, the number of pulses per cycle should be as small as possible.

Table 4.1 summarizes the required parameters to the pulsed proton beam. Figure 4.1 shows a typical time structure of the pulsed proton beam suited for the $\mu^- - e^-$ conversion experiment.

Table 4.1: Pulsed Proton Beam for $\mu^- - e^-$ experiment.

Beam Power	56 kW
Energy	8 GeV
Average Current	7 μA
Beam Emittance	10π mm·mrad
Protons per Bunch	$< 10^{11}$
Extinction	10^{-9}
Bunch Separation	1 μsec
Bunch Length	100 nsec

4.1.2 Pulsed Proton Beam at J-PARC MR

In order to implement the required proton beam, it is necessary to consider four major issues:

1. how to make the time structure of a pulsed proton beam,
2. how to control the proton beam emittance,
3. how to extract a beam to the beam line, and
4. how to achieve the required beam extinction.

It should be noted that a proton beam from the 3-GeV Rapid Cycling Synchrotron (RCS) cannot be used. The reasons are the following: (1) The muon facility at the 3-GeV RCS can have a proton target of limited thickness since it is placed upstream of the Neutron facility. (2) Placing a superconducting solenoid for pion capture,

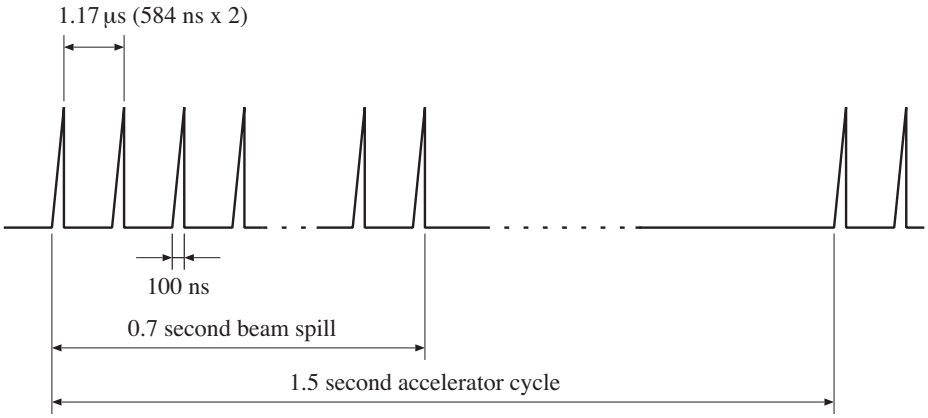

Figure 4.1: Bunched proton beam in a slow extraction mode.

surrounding a proton target, as described in Section 4.3, would block muons to the other muon beam line and have potential of conflicts to other muon users. (3) An expected beam intensity of about 10^6 muons/sec, when the concept of pion capture solenoid is given up and the current one target is shared by the other muon beam lines, is too small for our aimed intensity of 10^{11} muons/sec.

4.1.2.1 Beam Pulsing

In a standard operation scheme of J-PARC MR, the time period of every bunch is about 598 nsec (1.67 MHz) and a gap separation is about 300 nsec (*i.e.* 50 % filling). Since the delayed tail component of the beam related background extend almost 600 nsec after the primary proton timing, the present separation of pulses is too short for the $\mu^- - e^-$ conversion experiment. There are three possible solutions to this as shown in Table 4.2

In the first method, the only one of two RCS RF-buckets will be filled by chopping the proton beam in LINAC, and inject the filled bunch to the MR four times to form the four filled RF-bunches every each others in the MR. The advantage of this method is that J-PARC RCS and MR are both operated at the standard RF frequencies, thus no major modifications may be needed. The issues that has to be addressed would be a heat load to the RF chopper dump, and the proton leakage to the adjacent RF-buckets. It is note worth that the heat load problem would be solved if the prechopper is operated as planned.

In the second method, that is shown in Figure 4.2, RCS will be operated with RF harmonics being 1 ($h = 1$). This solves the heat load problem in the 1st method. It will also clear the potential problem of the proton-leak-to-the-adjacent-bucket in the RCS. In addition, the RCS tune shift will become a half since the space charge in the RCS is lower than the 1st method. However, it should be noted that the potential proton-leak-to-the-adjacent-buckets in the MR would be still there.

In both methods, the RF harmonics of MR could be changed to 8 instead of 9. This increases the pulse separation to 1.3μsec, and makes it equally divided. This

equally-division helps to design external extinction device. We prefer the 2nd method with h=8 as the baseline of our design.

In order to address the proton leak in the MR, the RF harmonics in the MR could be changed to 4 instead of 8. However, it needs major modification of RF cavities. The bunch length might be longer thus has to be shortened right before the extraction. This 3rd method would be a final concern.

Table 4.2: J-PARC MR bunching scheme. N_h is the number of RF harmonics, N_b is the number of filled bunches.

Method	RCS		MR		Difficulty	Extinction	Note
	N_h	N_b	N_h	N_b			
1	2	1	9(8)	4	Easy	Bucket Leak (RCS,MR)	Heat Load
2	1	1	9(8)	4	Moderate	Bucket Leak (MR)	
3	1	1	4	4	Higher	Good	Major Work

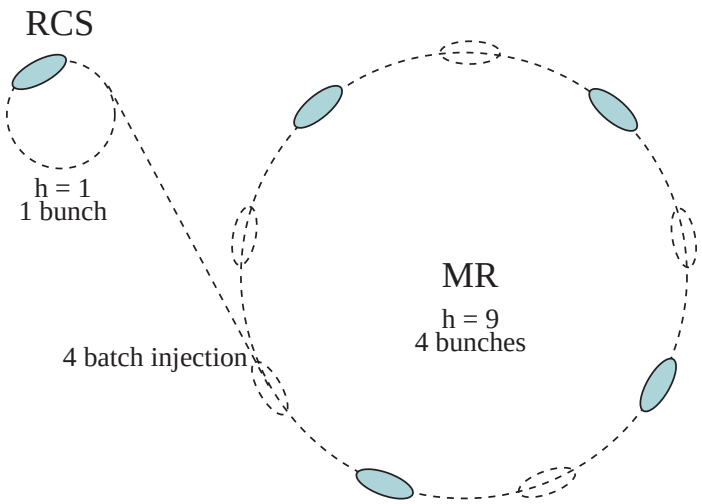

Figure 4.2: Machine cycle structure of the baseline method. It is also possible to have $h = 8$

4.1.2.2 Emittance Control

The proton energy that we will use is about 8 GeV. This is almost factor 4 smaller than the standard energy of the J-PARC MR (30 GeV). Because of this, the adiabatic dumping effect of the beam emittance in the MR is smaller than the standard energy operation. The vertical beam emittance of 8 GeV beam with the standard operation becomes 40πmm·mrad, which includes an emittance growth factor of ~ 2 due to space charge force.

In order to solve the problem, we propose the following scheme. Firstly, the number of protons in a bunch would be reduced to prevent the emittance growth by space charge effect, but the cycle repetition would be increased since the time for acceleration and extraction can be shorter. The cycle time would be as short as 1.5 sec. The estimated number of protons is 1.6×10^{13} protons per bunch, thus the beam current will be 7 μA. Secondary, RCS painting area would be reduced down to 93π mm·mrad from a standard size (144π mm·mrad) and set the aperture of the 3-50BT·MR collimator to 23π mm·mrad, which is smaller than the standard setting (54π mm·mrad).

4.1.2.3 Extraction

The number of pulses extracted to the beam line should be larger than 100 pulses per cycle in order to reduce the number of protons in a pulse. Because of this, a fast extraction would not be used as the 1st choice, but the bunched slow extraction has to be considered. Then, the number of pulses per cycle should be as small as possible to reduce the cosmic-ray background. If the number of pulses is just 100 and the pulse duration is 1.17 μsec, it will take only 0.1 msec of the slow-extraction length but this is practically too short from the point of view of the slow extraction technique.

The potential issues that has to be addressed for shortening the slow-extraction time are two folds. One is the time response of the slow extraction magnets. The slow extraction needs a ramping of the magnets, thus the time response will limit the slow-extraction length. The other is an extraction efficiency.

From these potential limitations, a 0.1 sec of the slow-extraction length would be a possible choice for the MR. At this slow-extraction length, average beam current could be 70% higher and the run time could be shorter or statistics sensitivity might be higher with the same run time. The experiment can start with the standard length (0.7 sec), and the actual length should be optimized by looking at the balance of detector rate, physics background and MR performance.

4.1.2.4 Extinction

The beam extinction between the beam bunches is of critical importance. For the MECO experiment [38], some tests to measure the proton extinction were done at BNL-AGS. In the test, one RF bucket was filled and accelerated to 24 GeV and slow-extracted the bunches. The rate of neutral kaons with respect to the RF bucket was measured. Figure 4.3 shows the relative intensity as a function of time with respect to the filled bucket. The proton extinction between buckets is below 10^{-6} and in empty buckets is of order of 10^{-3}. After this, the second test by using the E787 detector was done. This time, the beam energy was only 7.4 GeV. They obtained the extinction being at 10^{-7}. Our speculation to the difference between the 1st test and the 2nd test is that the existence of a transition energy. The transition energy of AGS is about 8 GeV, and the RF phase should be jumped at the transition energy. This might cause the proton leakage to the adjacent buckets. From that point of view,

there is an advantage in J-PARC MR, since the transition energy does not exist for MR. We could hope to achieve 10^{-7} of the extinction at J-PARC MR without serious difficulties.

The conclusion drew by AGS people at that time was that the proton extinction of 10^{-9} is unlikely to be achieved by just tuning of the AGS, and two possibilities to improve the extinction were proposed. One is to install an external extinction device in the proton transport line. The external extinction device consists of two AC-dipoles, a collimator and quadrupole magnets. The off-timing beam will be kicked by AC-dipole and stopped by collimator. The beam passed thought the collimator gap will be matched back to the beam line axis by the 2nd AC-dipole.

The second method is to involve a system of kickers in the ring. This system has an advantage that the kickers run continuously during acceleration and kick beams many times, and therefore the kicking field can be relatively small. They proposed the two magnet system in the AGS ring, one of which is running at a slow frequency (60 kHz for AGS) to destabilize the beam and the other one is running at a fast frequency (740 kHz for AGS) to preserve the stability of the beam in the filled RF bunches. The field integral of this kicker is adjusted to be equal and opposite in magnitude so as that the filled bucket pass through when it fires.

At the J-PARC MR, we have third method to improve the extinction, in which the MR will be operated at RF harmonics 4 (Method 3). There will be no more

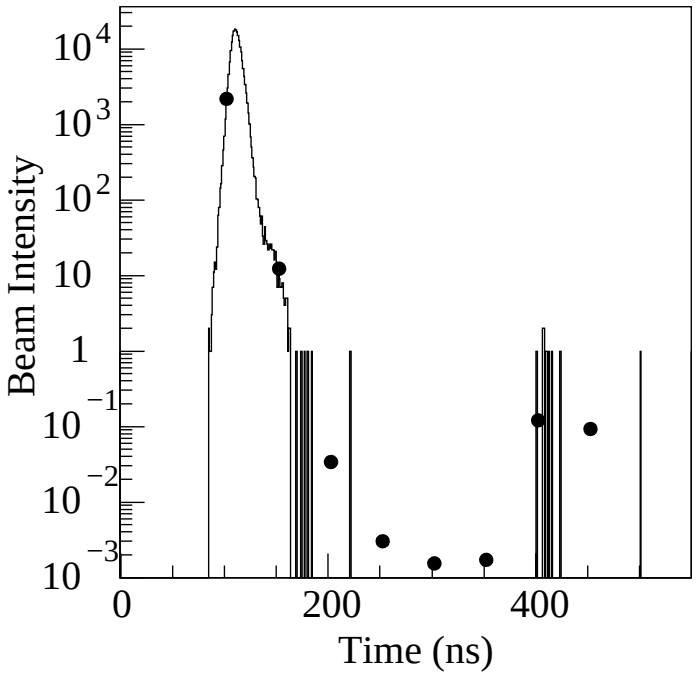

Figure 4.3: Results of the proton beam extinction measured at BNL-AGS. The beam intensity as a function of time with respect to pulses in the bunched beam extracted from the AGS. The solid histogram and dots are the results from the measurements of with a QVT and scalers, respectively.

"empty buckets", so the bucket leakage may not happen.

The actual actions to the extinction improvement strongly depend on the mechanism of the extinction degradation. If the bucket leak occurs in the RCS, the RF harmonics of the RCS has to be one. If the bucket leak occurs in the MR during the acceleration, we may need the kickers in the ring or four-harmonics operation or external extinction device or all of them. If the bucket leak occurs during the slow extraction process, neither kicker in the ring nor the four-harmonics operation can help. In that case, the external extinction device is the only choice.

Table 4.3: J-PARC Operation Parameters. Linac energy is assumed to be 400 MeV.

Item	Standard Slow	Pulsed Slow	Pulsed Fast
Proton Energy (GeV)	30	8	8
No. of Protons in a Bunch	0.4×10^{14}	0.16×10^{14}	0.096×10^{14}
Average Current (μA)	15	7(12†)	7
Beam Emittance (mm·mrad)			
Vertical			
RCS Injection	144π	93π	93π
MR Injection	54π	23π	23π
Flat Top	10π	10π	10π
Extracted Beam	10π	10π	10π
Horizontal			
RCS Injection	144π	93π	93π
MR Injection	54π	23π	23π
Flat Top	$<10\pi$	$<10\pi$	10π
Extracted Beam	$<10\pi$	$<10\pi$	10π
RCS Harmonics	2	1	1
RCS Bunches	2	1	1
Batches RCS→MR	4	4	4
MR Harmonics	9	9 or 8	9 or 8
MR Bunches	9	4	4
Cycle Time (sec)	3.53	1.5(0.9†)	0.9
Injection Time (sec)	0.17	0.17	0.17
Acceleration Time (sec)	1.96	0.35	0.35
Extraction Time (sec)	0.7	0.7(0.1†)	0.1
Setup Time (sec)	0.7	0.28	0.28
Extraction	DC Slow	Bunched Slow	Fast
Number of Pulses	—	0.6M(0.1M†)	4
Pulse Separation (μsec)	—	1.17	1.17
Pulse Length (nsec)	—	100	100
No. of Protons in a Pulse	—	10^8($10^{9\dagger}$)	3.8×10^{13}

† Numbers in parentheses are those for short slow-extraction time length.

4.2 Proton Target

4.2.1 Pion Production by Proton Incident

Experiments on searching for $\mu^- - e^-$ conversion would use low-energy muons which can be stopped in a target. These low-energy muons are mostly produced by in-flight decay of low energy pions. Therefore, low-energy pions is of interest. At the same time, high-energy pions, which could potentially cause background events, should be eliminated. In order to study the pion production and pion capture by solenoid, Monte Carlo simulations have been performed by using two different types of hadron codes, namely MARS and GEANT3 with FLUKA. Note that the MARS code is a hadron production code developed at Fermilab.

Fig.4.4 shows the momentum spectra of π^- produced from a graphite target. It can be seen that the maximum of transverse momentum (p_T) is around 100 MeV/c for a longitudinal momentum (p_L) of $0 < p_L < 200$ MeV/c for both the forward- and backward-scattered pions. The maximum of the total momentum for the backward-

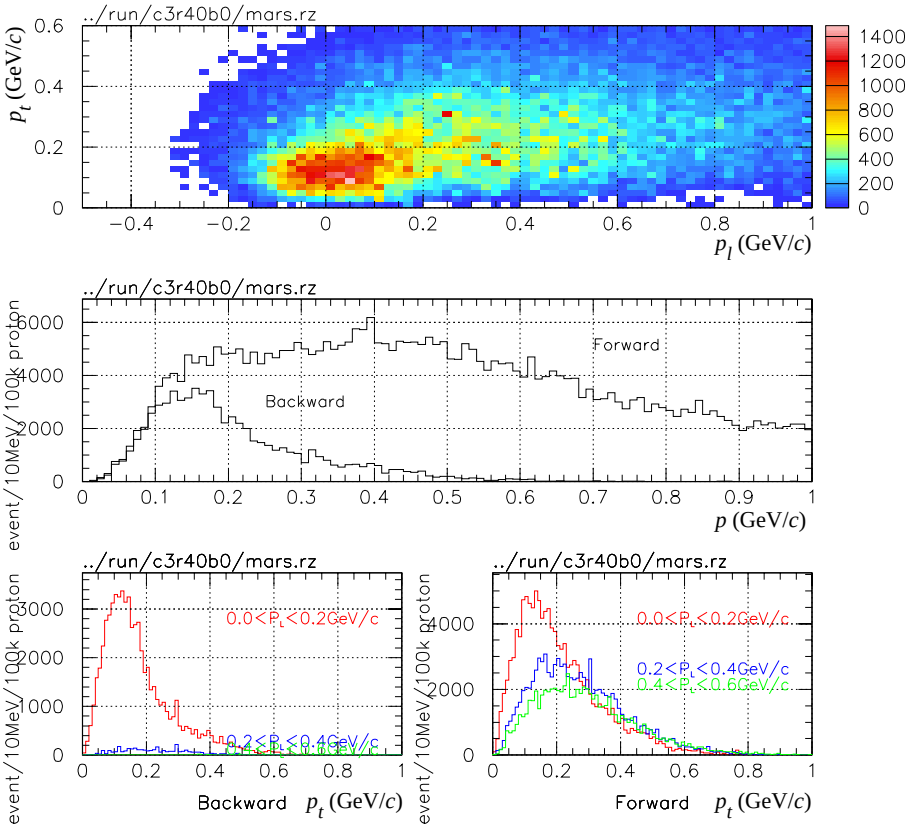

Figure 4.4: Pion production in a graphite target. (top) Correlation between p_L and p_T. (middle) Total momentum distributions for forward and backward π^-s. (bottom) p_T distributions for $0 < p_L < 0.2$ GeV/c, $0.2 < p_L < 0.4$ GeV/c, and $0.4 < p_L < 0.6$ GeV/c.

scattered pions is about 120 MeV/c, whereas that for the forward-scattered pions is about 200-400 MeV/c. It can also be seen that high-energy pions are suppressed in the backward direction. The low energy pion yields would be not so different between forward- and backward direction. In conclusion, backward pions are less contaminated by high energy pions while retaining the low energy pion yields. For those reasons, it has been decided to collect pions emitted backward with respect to the proton beam direction.

Figure 4.5 shows yields of pions and muons as a function of proton energy. As seen in Fig.4.5, the pion yield increases almost linearly as proton energy, therefore by proton beam power. Also it is seen that at a very high proton energy (> 30 GeV), the pion production yield starts to be saturated.

The choice of proton energy can be determined from the pion production yield and the background consideration, in particular of the proton beam extinction and antiproton induced background. At this moment, our choice of proton energy is 8 GeV, as described in Section 4.1. It is the same as in the MECO/Mu2e experiments.

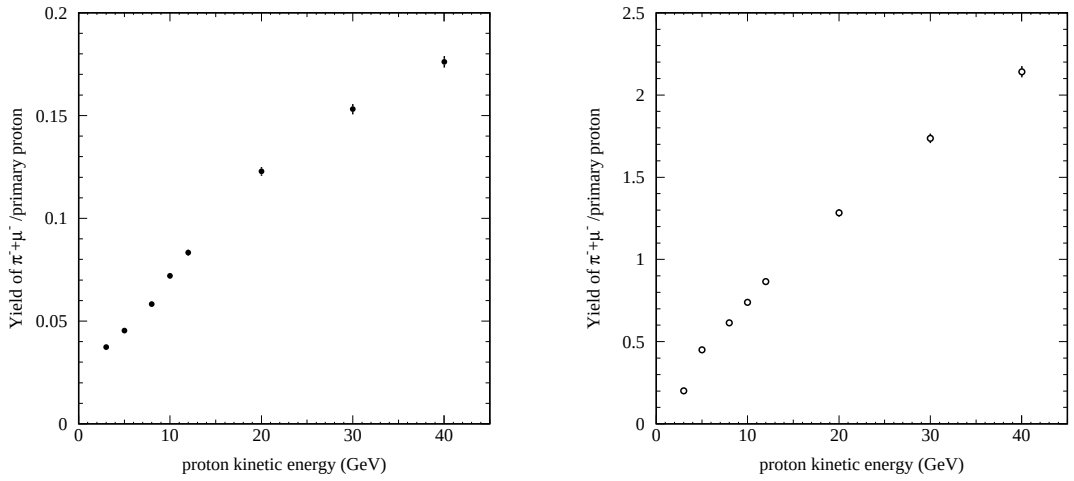

Figure 4.5: Yields per proton of backward pions and muons (in left) and forward pions and muons (in right) from a graphite target in a magnetic field of 5 Tesla as a function of proton energy.

4.2.2 Proton Target for Pion Production

Pion production cross section is higher in a heavier material than a light one; it is almost 3 times larger for tungsten than graphite. However, if it is a metal target, it would melt down when a high power proton beam hits, and therefore target cooling is necessary. For examples, T1 target in the J-PARC NP hall is designed to be a rotating wheel made of Ni with water cooling.

The proton target for pion production in this experiment will be placed inside the superconducting solenoid magnet. Thus, a rotating wheel target could not be adopted. The current target design for this experiment is based on that for T2K experiment; a graphite rod target cooled by He gas. However it is known that replacement of graphite targets in months is needed owing to radiation damage on deterioration of its specific heat. Alternative solution would be the target proposed in the MECO/Mu2e experiments; water cooled tungsten rod, since a proton beam power would be almost the same.

Figure 4.6 shows pion yield as a function of target length. The pion yield at low energy is almost proportional to the target length up to about 60 cm for graphite (which corresponds to 1.5 interaction lengths). Although the longer target provides more pion yields, it should be optimized considering the radiation load to the pion capture solenoid in which the target is embedded. In the current design, the target length is 60 cm.

The yield of pions at low energy decreases as the radius of the target increases. This would be explained by the absorption of pions at low energy. It was found that the optimum radius is about 2 cm for a graphite target. In summary, the target for this experiment will be a graphite target with 1.5 times of the interaction lengths and 2 cm radius, cooled by either water or He gas.

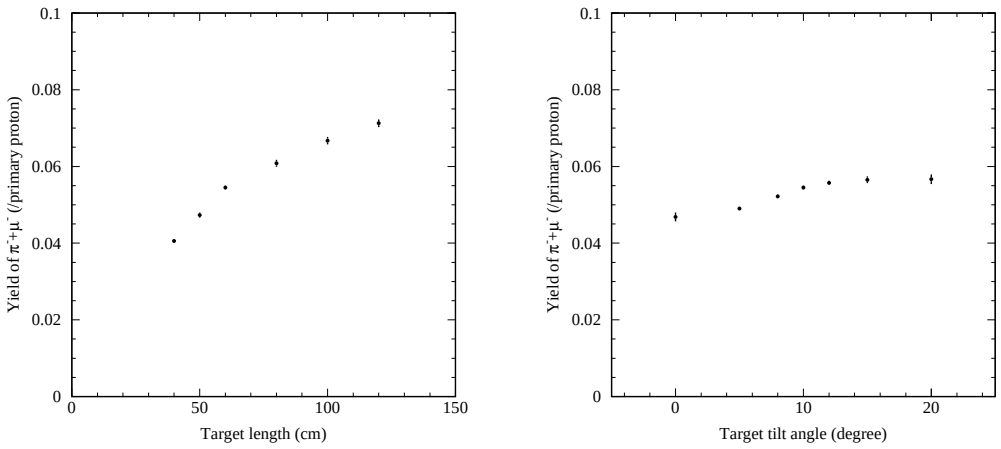

Figure 4.6: Yields of backward pions from a graphite target in 5 Tesla magnetic field as a function of target length (left figure) and target tilt angle (right figure).

Pion production target is embedded in solenoid magnet to capture and transport generated pions in the magnetic field. The target should be tilted with respect to solenoid axis to inject proton beam into solenoid magnet. Figure 4.6 shows the pion yields as a function of tilt angle of a graphite target. As seen in Fig.4.6, the pion yield is almost saturated around at tilting angle of 10 degree. The deposit energy in a graphite target is 2 kW for 8 GeV protons with 7 μA.

It is note worthy to mention that the improvement of the muon yield is possible by the following modifications. These improvements become feasible if the radiation effect to the superconductive solenoid coil is relaxed.

- A 100 cm graphite target can improve pion yields by 20%,
- the collection efficiency of pion capture can be improved by 20% if the target is placed in the graded field region,
- a factor 2 of the improvement with heavy metal target like MECO/Mu2e.

4.3 Pion Capture

4.3.1 Pion Capture in a Solenoid Magnetic Field

To collect as many pions (and cloud muons) of low energy as possible, the pions are captured using a high solenoidal magnetic field with a large solid angle. Figure 4.7 shows a layout of the pion capture system, which consists of the pion production target, high-field solenoid magnets for pion capture, and radiation shield. In this case, pions emitted into a half hemisphere can be captured within the transverse momentum threshold ($p_t^{\max}$). This $p_t^{\max}$ is given by the magnetic field strength (B) and the radius of the inner bore of solenoid magnet (R) as

$$p_T^{\max}(\mathrm{GeV}/c) = 0.3 \times B(\mathrm{T}) \times R(\mathrm{m})/2. \tag{4.1}$$

The optimization of the magnetic field of the capture solenoid was performed by looking at the muon yields at 10 m downstream from the target; the exit of the transport solenoid located at the downstream of the capture solenoid magnet. Note that the most of pions decay into muons in the transport solenoid magnet. It was observed that the higher the pion capture magnetic field is, the better the muon yield at the exit of the pion decay system becomes. Therefore, a higher magnetic field is preferable. According to Fig.4.4, placing $p_T^{\max}$ at around 200 MeV/c would be sufficient. Furthermore, since we are interested in the muon momentum being less than 75 MeV/c, the solenoid magnet with the bore radius of 15 cm can accept most of the parent pions for such low-energy muons. Detailed optimization of the bore radius strongly depends on the available technology of the superconducting solenoid magnet. In the current design, we employ conservative design values, namely of $B = 5$ T, $R = 15$ cm and the length of 1.4 m.

4.3.2 Adiabatic Transition From High to Low Magnetic Fields

Since the pions captured at the pion capture system have a broad directional distribution, it is intended to make them more parallel to the beam axis by changing a magnetic field adiabatically. From the Liouville theorem, a volume in the phase space that beam particles occupy does not change. Under a solenoidal magnetic field, the

relation between the radius of curvature (R) and the transverse momentum (p_t) leads to the relation given by

$$p_t \times R \propto \frac{p_t^2}{B} = \text{constant}, \tag{4.2}$$

where B is a magnitude of the magnetic field. Suppose the magnetic field decreases gradually, p_t also decrease, yielding a more parallel beam. This is the principle of the adiabatic transition. Namely, when a magnetic field is reduced by a factor of two, p_t decreases by $1/\sqrt{2}$. On the other hand, since

$$p_t \times R \propto B \times R^2 = \text{constant}'. \tag{4.3}$$

the radius of curvature increase by a factor of $\sqrt{2}$. Therefore, the inner radius of a magnet in the pion decay section has to be $\sqrt{2}$ times that of the pion capture. With the cost of a beam brow up, a pion beam becomes more parallel. Furthermore, it is not effective in reality to have a long magnet with a high magnetic field, and a magnetic field has to be lowered at some point. Figure 4.9 illustrates the principle of adiabatic transition.

4.3.3 Pion Capture Solenoid Magnet

We aim to develop the system that can be operated under 500 W of the heat load. Radiation shield should be installed between the target and the superconducting coil. This will further increase the total radius of the superconducting solenoid magnet. The radiation heat load to superconducting coils placed behind the 30 cm-thick radiation shield of tungsten is the level of 2×10^{-5} W/g for 8 GeV proton beam with 7 μA. The radiation heat comes mostly from neutrons.

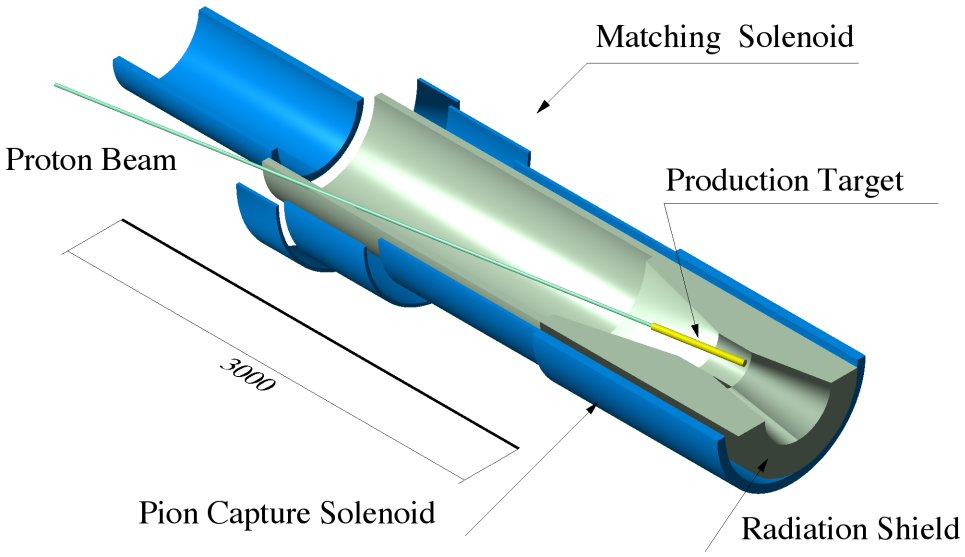

Figure 4.7: Layout of the pion capture system, which consists of the pion production target (proton target), the pion capture solenoid magnets, and its radiation shield.

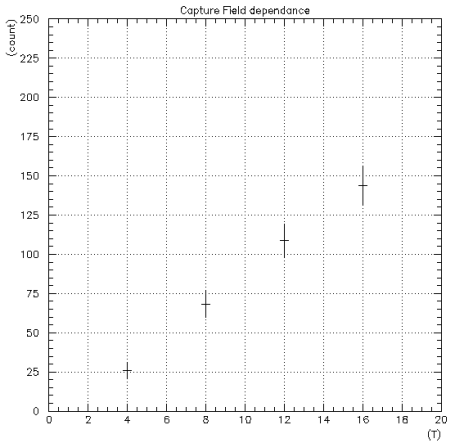

Figure 4.8: Muon yields at 10 m from the entrance of the pion decay system as a function of magnitudes of a pion capture field.

If copper is used as the stabilizer of the superconducting coils, a total thickness of the coil might be about 20 cm or more[3], and a total impact on the 4.5 K refrigeration load is over 1 kW. In order to overcome this difficulty, we have started design works using Al-stabilized superconducting coil.

4.3.3.1 Superconducting Coil

To reduce energy deposit by neutrons radiated from pion production target, Al-stabilized superconducting coil is employed. Figure 4.10 shows a cross section view of a coil conductor. It consists of 32 strands of NbTi super-conductor with 1.28 mm diameter. The dimension of the conductor is 30 cm in height and 5 cm in width. The fractions of each composition are 19%, 34% and 46% by weight for NbTi, Cu and Al, respectively. The density of the conductor is 4.0 g/cm^3.

4.3.3.2 Layout of Pion Capture Solenoid

Figure 4.10 shows a schematic view of the system of pion production and capture. It consists of a proton target, a surrounding radiation shield, a superconducting solenoid magnet for pion-capture with a 5 Tesla magnetic field, and matching section connected to the transport solenoid system with a 2 Tesla field. The radiation shield is inserted between the pion production target and the coil which generates 5-Tesla magnetic field. To achieve low heat load enough below 100W, 30 cm-thick tungsten shield is necessary. An inner radius of the 5-Tesla coil is 50 cm. The inner bore of the shield is tapered to keep it away from beam protons and high-energy pions, which are scattered forward. To collect backward-scattered pions, proton beam should be injected through the barrel of the solenoid, and should be tilted with respect to the

[3]For example, see "MECO Superconducting Solenoid System Conceptual Design Report"[40]

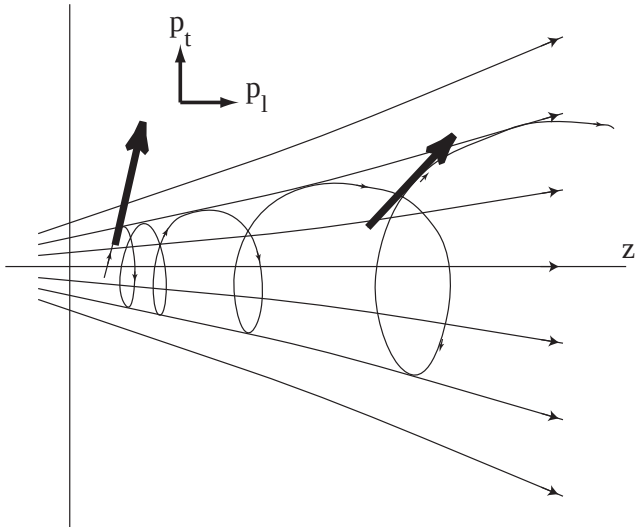

Figure 4.9: Adiabatic transition from a high magnetic field to a low magnetic field. This adiabatic transition reduces the magnitude of transverse magnetic field.

solenoid axis by 10 degrees. The coil near proton beam duct should have a larger radius to escape from a beam halo. In the current design, the coil is placed more 10-cm far from the beam axis.

The direction backward-scattered pions captured in 5-Tesla magnetic field is focused forward in degrading magnetic field down to 2 Tesla. The matching section has a large bore due to increasing diameter of pion trajectory in the tapered magnetic field, and also to contain both the coils of matching and capture section in the large cryostat.

4.3.3.3 Magnetic Field in Pion Capture Solenoid

To achieve 5-Tesla magnetic field and low radiation heating, the coil is wound in 2 layers, which thickness is only 6 cm in total, and current density in the conductor should be 80 A/mm^2. The magnetic field distribution is shown in Fig. 4.11. The stored energy of the capture solenoid is 12.3 MJ. The ratio of the energy to the mass of super-conductor, E/M, is 12.5 kJ/kg, and the critical field is 8.4 T. Therefore, it can be said that the capture solenoid of the design with Al-stabilized superconducting coil is capable with presently achievable technique.

4.3.3.4 Heat Load of Pion Capture Solenoid

From the MARS-simulation study on the radiation shielding, a thickness of the radiation shield made of tungsten should be about 30cm or more, if it is required the heat load on the superconducting coil should be less than 100 W. Figure 4.12 shows the energy deposit distribution in the solenoid system obtained from the simulation. In the current design, deposit energy in the radiation shield around the target is 35 kW

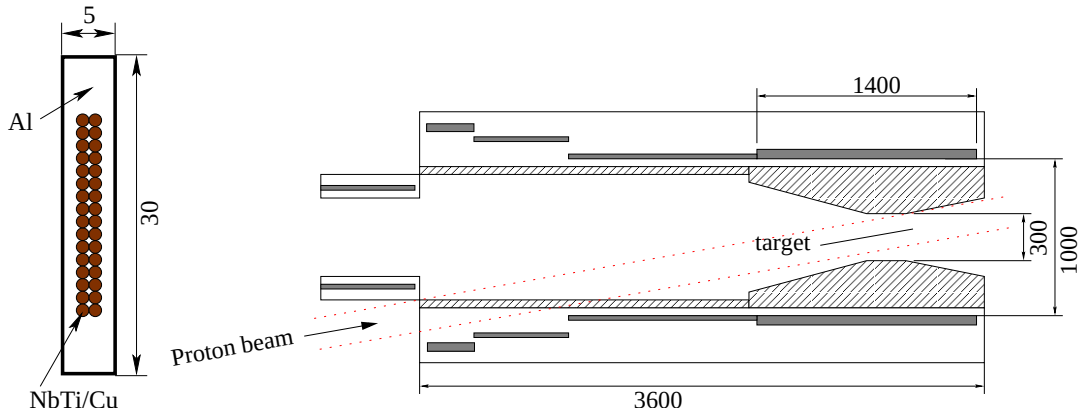

Figure 4.10: Left: Cross section of superconducting coil for capture solenoid. Right: Schematic layout of the capture solenoid system. Shaded area is radiation shield made of tungsten. Gray regions represent superconducting coil. A proton beam is injected from lower-left of the figure, and captured pions are transported towards left. Dimensions are in mm.

for 8 GeV proton beam with 7 μA. Therefore, the shield material should be cooled by water. Heat load on the coil of capture section is calculated to be only 10 W. Since it is well-below our requirements, the coil can be cooled by indirect cooling, which is commonly used for thin superconducting solenoid magnet.

4.4 Muon Beam Line

Pions and muons are transported to a muon-stopping target through the muon beamline, which consists of curved and straight solenoids. The key requirement for the muon beamline is that it should be possible to select the electric-charge and momentum of beam particles. In addition, it is required to provide a high-efficiency transportation of muons having a momentum of around 40 MeV/c. At the same time, it is necessary to eliminate energetic muons having a momentum larger than 75 MeV/c, since their decays in flight would produce spurious signals of $\sim$105 MeV electrons. Therefore, such energetic muons and other unwanted particles are strongly suppressed before the stopping target using the curved solenoid.

A schematic layout of the muon beamline including the capture and detector sections is shown in Fig. 4.13. Tracking simulation studies were performed using a single-particle tracking code based on GEANT. The magnetic field of the solenoids can be computed using a realistic configuration of coils and their current settings.

4.4.1 Curved Solenoid

The selection of the electric-charge and the momentum of beam particles can be performed by using curved solenoids. It is known that, in a curved solenoid, the center of the helical trajectory of a charged particle drifts along the perpendicular

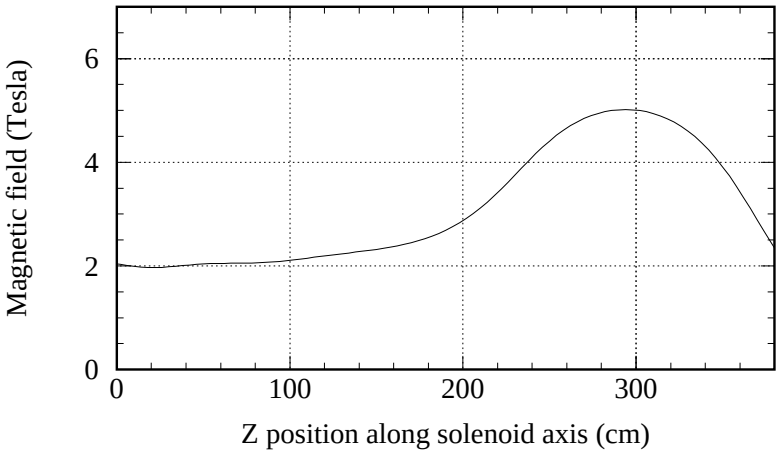

Figure 4.11: Magnetic field along solenoid axis of the pion capture system. The target is located at $z = 300$ cm in the figure, and pions are transported towards left-hand side.

direction of the curved solenoid plain, and the drift (D[m]) is given by

$$D = \frac{q}{0.3 \times B} \times \frac{s}{R} \times \frac{p_l^2 + \frac{1}{2}p_t^2}{p_l}, \tag{4.4}$$

where q is the electric charge of the particle (with its sign), B[T] is the magnetic field at the axis, and s[m] and R[m] are the path length and the radius of curvature of the curved solenoid, respectively. Namely, s/R is a bending angle. p_l and p_t[GeV/c] are parallel and transverse momentum respectively. Charged particles with opposite sign move in the opposite direction. This can be used for charge and momentum selection if a suitable collimator is placed after the curved solenoid. This type of curved solenoid magnets has been already adopted in the MECO (BNL-AGS E940) experiment. Unless two curved solenoids bent in opposite directions are installed, a dipole magnetic field to compensate for the drift of particles having the momentum of interest might be needed.

The momentum dispersion is proportional to the bending angle of the curved solenoid. The present design utilizes two curved solenoids with a bending angle of 90° in the same bending direction. They each have a magnetic field of 2 T and a radius curvature of 3 m. Adjustment of the inner radius of the solenoid works as the collimators and this design would bring down costs. To keep a center of trajectory of the low energy muons, compensative fields of 0.038 T for the first 90° and 0.052 T for the second one were applied. In the tracking simulation these, compensative fields are modeled as hard edge fields.

The inner radius is optimized to achieve both of the enough suppression power of unwanted particles and good stopping efficiency of the low-energy muons on the

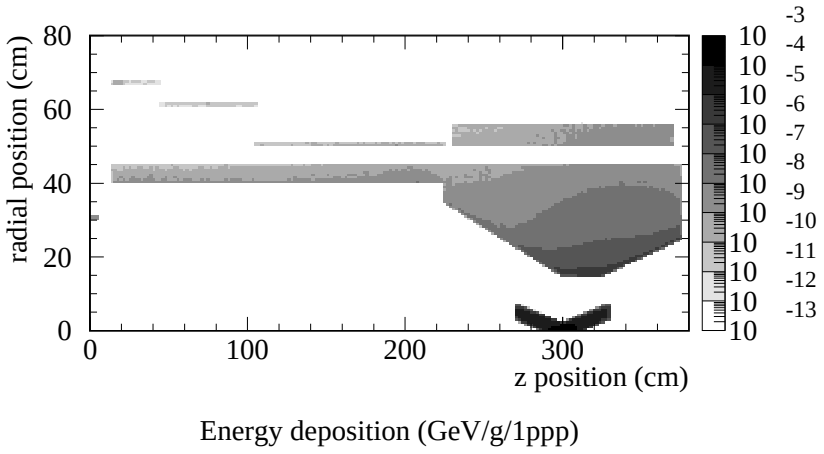

Figure 4.12: Distribution of energy deposit in the materials in the capture system in the unit of GeV/g per proton. The horizontal is z positions along the axis of capture solenoid, and the vertical indicates radial position from the central axis of the solenoids. A graphite target is located at $z = 300cm$ in the figure.

target. To determine this parameter a tracking simulation study was performed using a beam data set which made by MARS code with 5×10^5 protons on the production target. Figure 4.15 shows the yields of muons passing the beam line, that of stopped muon at the stopping target, and that of muon with higher momentum as a function of the inner radius of the solenoids. The target configuration used in this study is described in a later section. We take the inner radius of 175 mm as a baseline design, which has enough suppression power as mentioned in a later section.

4.4.2 Decay Solenoid

To let pions decay into muons, we need a long flight path. Also, to contain those pions and decay muons in a limited space, a long solenoid magnet is required. At the momentum of about 100 MeV/c, a mean decay length of pions is about 10 m, and therefore a flight length of 10 m is needed.

The present design has a straight solenoid of 1.2 meter long between the curved solenoid and the stopping target solenoid section. Therefore a total flight length before the stopping target is about 15 m. Spectrum of particles at the end of the decay solenoid for the inner radius of 175 mm are shown in Fig. 4.16. The pion yield of $1\times10^{-5}\pi$/protons are obtained. It looks like sufficient number in a point of view of a background estimation as shown in a later section.

It is note worth that the length of the decay solenoid section depends on the layout of the experiment in NP Hall. As shown in Chapter 7, a possible layout in the J-PARC NP-Hall has a long straight section of the decay solenoid such as 10$\sim$20 m.

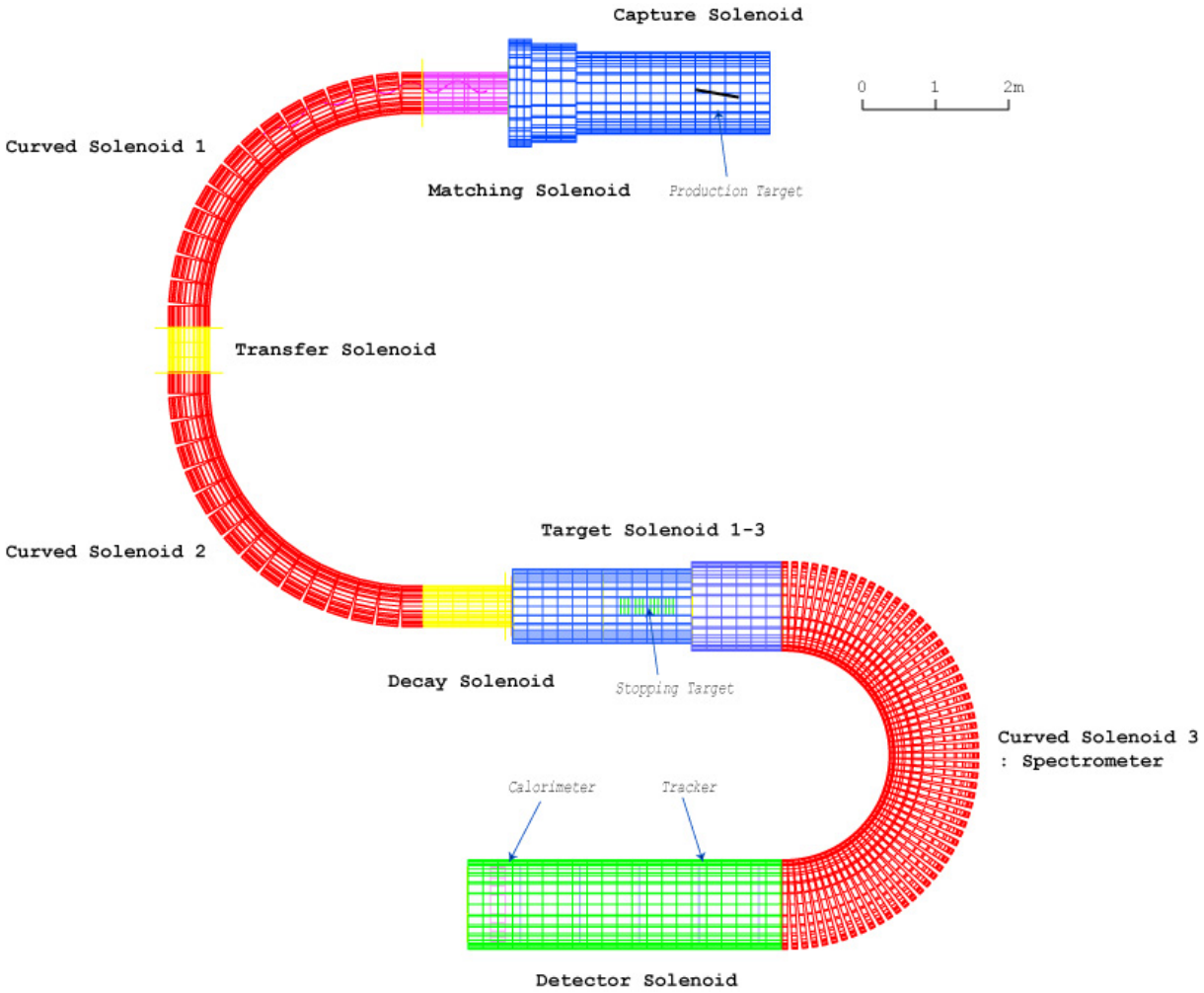

Figure 4.13: Present design of solenoid channel used in tracking studies.

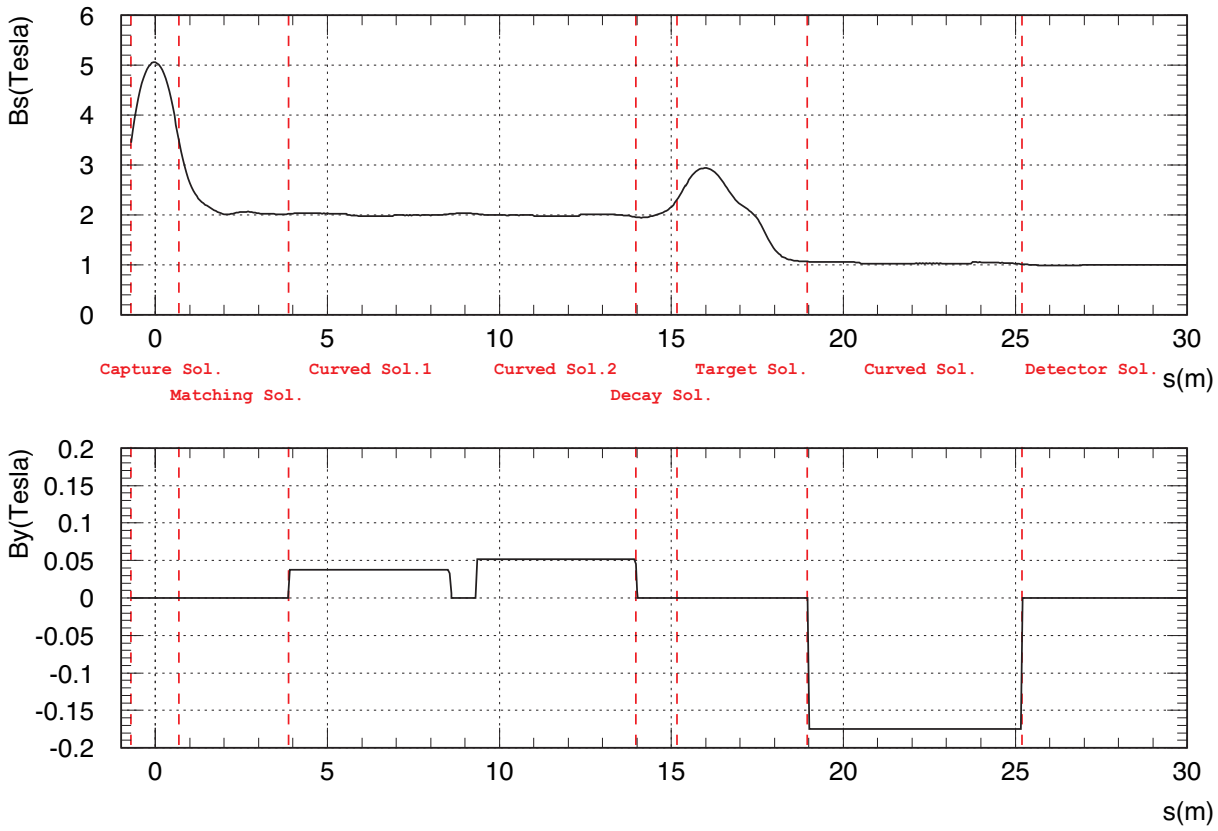

Figure 4.14: The magnetic field configuration of the solenoid channel from the capture section to the detector section of the present experiment. B_s is a central magnetic field of the solenoid magnets. B_y is a correction magnetic field.

It will be advantageous to have such a long decay solenoid section since pions may decay away while most of muons do not decay.

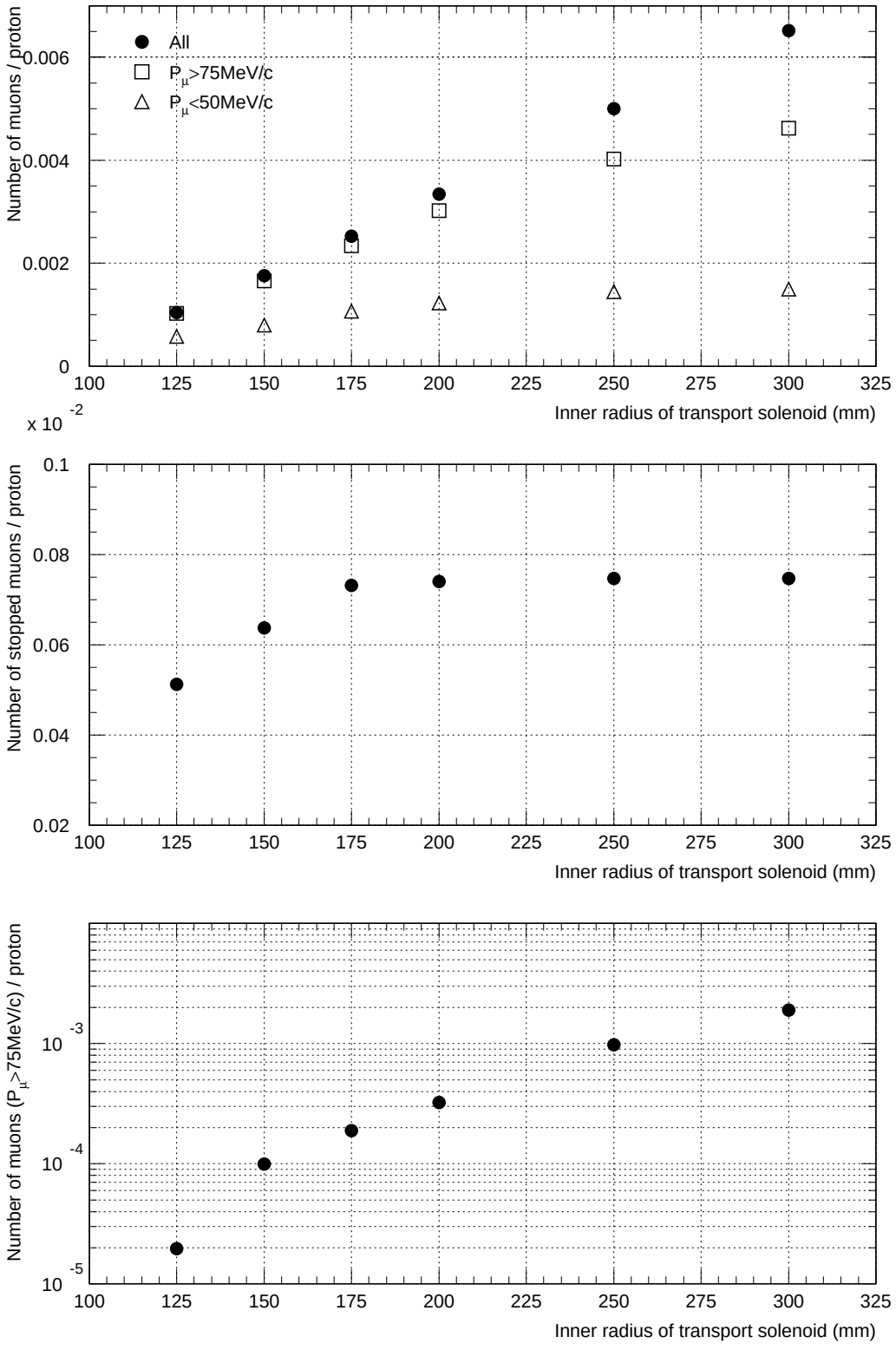

Figure 4.15: The yields of muons passing the beam line (top), that of stopped muon at the target (middle), and that of muon with higher momentum (bottom) as a function of the inner radius of the solenoids

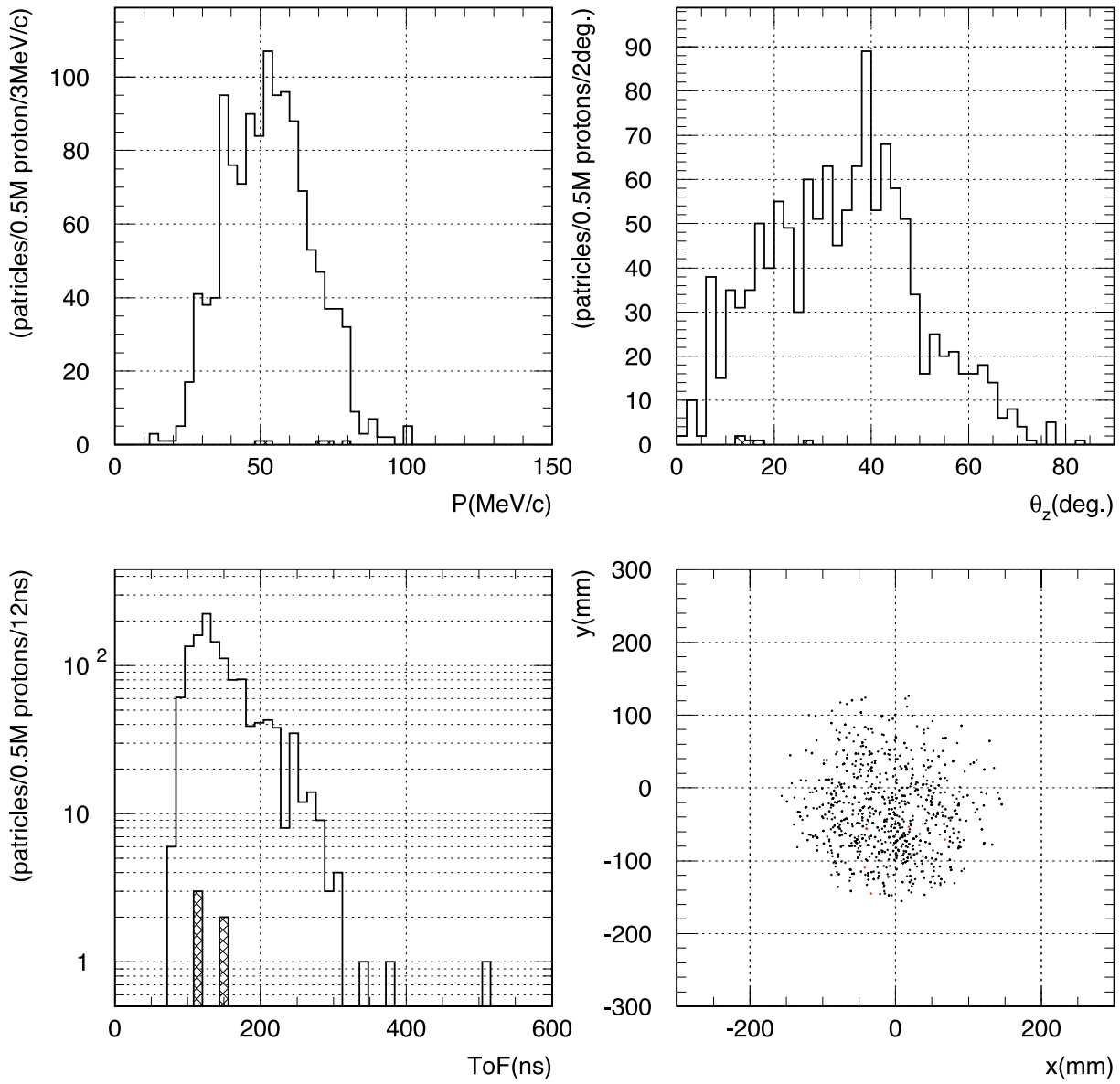

Figure 4.16: Plots for muons and pions (hatched histogram and red markers) at the end of the decay solenoid section. Total momentum (top-left), angle with respect to the axis of the solenoid channel (top-right), time of flight relative to the time when the proton beam hit the production target (bottom-left), and beam profile (bottom-right) are shown.

Chapter 5

The Detector

5.1 Overview

In this chapter, we describe a proposed detector for searching for $\mu^- - e^-$ conversion at a sensitivity of 10^{-16} in detail.

The sole role of the detector is to identify genuine $\mu^- - e^-$ conversion events from the huge number of background events. The signature of a $\mu^- - e^-$ conversion event is, as mentioned in Section 2.1, a mono-energetic ($\sim$105 MeV) electron emerging out of a muonic atom, which is formed by a muon stopped in a material. In contrast, background events have various origins. They can be rejected using various combinations of different methods associated with the muon beamline and the detector. The background event rejection will be explained in detail in Chapter 6.2. The observables that can be obtained from the signal electron are only momentum, energy, and timing. It is note worth that the detector being considered here is quite dif-

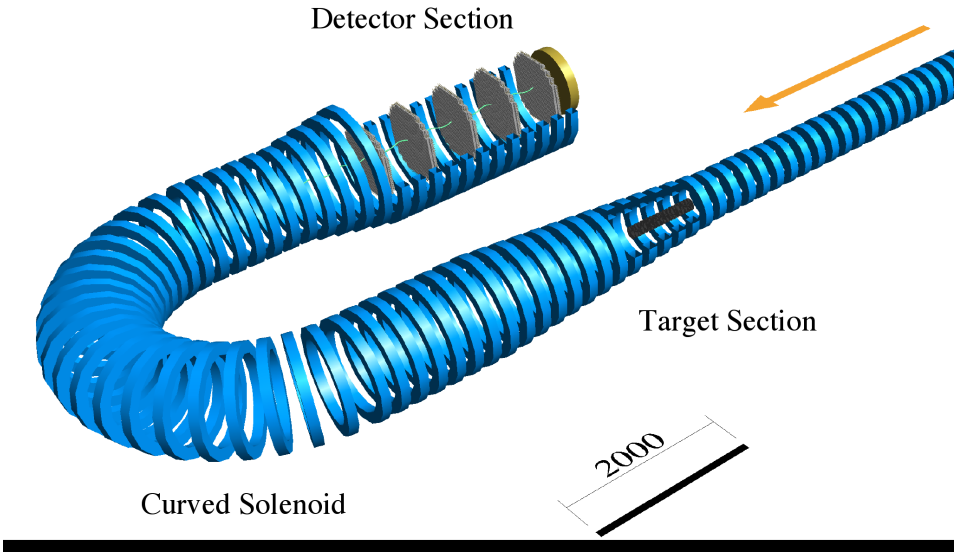

Figure 5.1: Setup of proposed spectrometer.

ferent from the one planned in the MECO experiment [38]. The COMET detector consists of three sections: target, curved solenoid spectrometer, and active detector sections. The target section is where a muon-stopping target is placed in a graded magnetic field. The curved solenoid spectrometer section transports electrons and other background particles with momentum selection power. Low energy electrons and background particles are blocked and do not reach to the active detector section. Neutral particles from the muon-stopping target will be also shielded from the active detector section. The third section, the active detector section, is to measure the momentum and energy of electrons.

5.2 Muon-Stopping Target Section

The muon-stopping target has to be designed to maximize the muon-stopping efficiency and the acceptance of the $\mu^- - e^-$ conversion electrons to the spectrometer. Also, it has to be designed to minimize the energy loss of the $\mu^- - e^-$ conversion electrons as they exit the target in order to improve the momentum resolution of the electrons. It is also important to make the target as small as possible to reduce any kinds of possible backgrounds.

5.2.1 Choice of $\mu^- - e^-$ Conversion Target

In this experiment, to eliminate background events arising from both prompt and late-arriving beam particles, a detection window opens about 700 nsec after the primary proton pulse, as shown in Section 5.6. Therefore, it is not suitable to use heavy materials for which the lifetime of muonic atoms is short. Table 5.1 shows a comparison between several materials. We have decided to use aluminum for a muon-stopping target.

Table 5.1: Lifetimes and relative strengths of $\mu^- - e^-$ process for typical materials.

	aluminum	titanium	lead
Atomic number	13	22	82
Lifetime of muonic atoms (μsec)	0.88	0.33	0.082
Relative branching ratio	1	1.7	1.15

A branching ratio of $\mu^- - e^-$ conversion processes, $B(\mu^- + N \rightarrow e^- + N)$, increases as an atomic number Z increases, and then saturates above $Z \simeq 30$, and decreases again for $Z > 60$. As for the photonic diagrams, the branching ratio for aluminum (Z=13) is smaller than titanium ($Z = 22$), but the ratio is only a factor of 1.7.

5.2.2 Configuration of Muon-Stopping Target

A configuration of a muon-stopping target is important to improve an experimental sensitivity and suppress backgrounds. Major parameters to be considered are thickness, size (such as a diameter), number of layers, distance between disks (spacing), and a magnetic field strength and magnetic field gradient. We have performed Monte Carlo simulations for various target configurations. The tentative target configuration we obtained is shown in Table 5.2.

Table 5.2: Configuration of Muon Stopping Target

Material	aluminum disk
Disk Radius	100 mm
Disk Thickness	200 μm
Number of Disks	17
Disk Spacing	50 mm

A magnetic field strength and gradient at the stopping target region is also very important. Especially, a graded magnetic field at the target location is indispensable condition. The first reason is to increase the acceptance by using mirroring effect. The second reason is to align the electron flight direction along the solenoid axis. This increases the transmission efficiency of the curved solenoid spectrometer section.

Fig. 5.2(Left) shows the baseline configuration of a graded magnetic field in the stopping target region. Monte Carlo simulations were carried out to study the stopping efficiency of muons for this configuration. Fig. 5.2(Right) shows the momentum distributions of the muons approaching the target (open histogram) and those stopped by the target disks (shaded histogram). A muon-stopping efficiency of 0.29 was obtained.

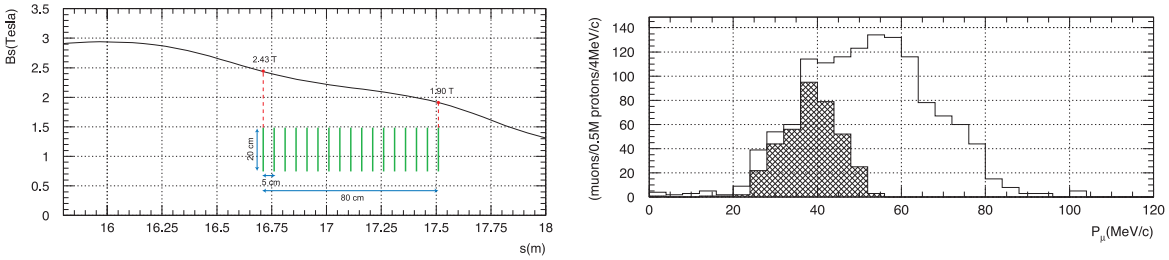

Figure 5.2: (Left) Distribution of a graded magnetic field over the target region. (Right) Momentum distributions of muons approaching the target (an open histogram) and those stopped by the muon-stopping target (a shaded histogram).

The Monte Carlo simulations performed here includes muon beamline, thus the effect of the momentum selection by the curved section as well as the potential mirror-back effect of the muons at the entrance of muon-stopping target section, where the field strength increases from 2 T to 3 T, are all considered properly.

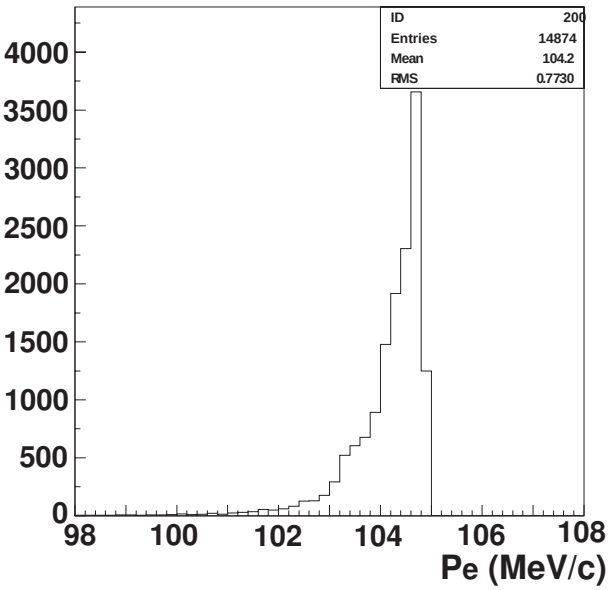

Figure 5.3: Momentum distribution of the Monte Carlo events of $\mu^- - e^-$ conversion signals with energy loss in the muon stopping target.

5.2.3 Energy Loss of Outgoing Electrons

Fig.5.3 shows momentum distribution of the outgoing electrons of 105 MeV/c generated in the muon stopping target, which is simulated by GEANT Monte Carlo simulation. It is found that an average energy loss is about 0.4 MeV.

5.3 Curved Solenoid Spectrometer Section

The electron transport system adopts curved solenoids to remove charged particles of low momentum because rejection of background events is necessary to reduce single counting rates of the detection system. The transport system consists of superconducting curved solenoids with a collimator inside the solenoid.

Many background particles are generated after the muon stopping target. They come from the stopping process in the target, contamination in the beam, and so on. These background rate is so high that they have to be suppressed so as the electron detector to work. The background rate is mostly dominated by DIO (muon decay in orbit) electrons and its energy spectrum has distribution to the high energy region near that of the conversion electrons (105 MeV). Figure 5.4 shows the relation between energy threshold and DIO events with electron energy larger than the threshold energy per one muon-stopping event in the target. The DIO event rate in the detector region will be reduced greatly by the momentum separator with a high energy threshold. For example, expected DIO event for one stopping muon is about 10^{-8} for the energy threshold of 80 MeV as shown in Fig. 5.4. In that case, the detection rate is estimated to be of the order of 1 kHz for 10^{11} muons per second in the muon-stopping target.

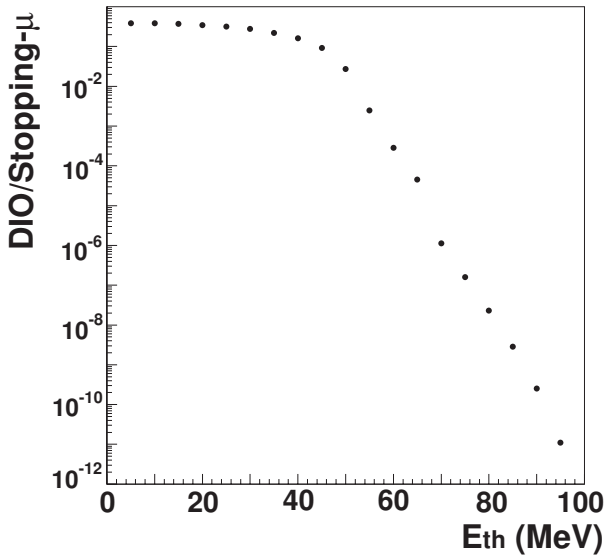

Figure 5.4: Energy threshold v.s. a number of DIO events with electron energy larger than the threshold energy per one muon stopping in the target.

5.3.1 Curved Solenoid and Correction Fields

The curved solenoid spectrometer is a magnetic system to select a charged particle with a desired momentum. The principle is just the same to that used in the muon beamline. When a charged particle is trapped in a solenoidal magnetic field, it moves in a helical trajectory around the magnetic field. Then if the solenoid is curved, the magnetic field is in toroidal shape, the center of helical trajectory of the charged particle drifts to a direction perpendicular to the bending plain. A drift distance D is given by

$$D = \frac{1}{qB_0}\left(\frac{s}{r_0}\right)\left(\frac{p_\parallel^2 + \frac{1}{2}p_\perp^2}{p_\parallel}\right), \tag{5.1}$$

where B_0, r_0, s, $p_\parallel(p_\perp)$ are a magnetic field, a radius of the toroid, a path length along the particle's central orbit, and particle's parallel (perpendicular) momenta, respectively.

This drift can be compensated by an dipole field superimposed along the drift direction. The strength of the compensating dipole field is represented by

$$B_{aux} = \frac{B_0 v_\parallel}{\omega_B r_0}\left[1 + \frac{1}{2}\left(\frac{p_\perp}{p_\parallel}\right)^2\right],$$

where $\omega_B = qc^2B_0/E_e$. For example, if $r_0 = 2$ m, one may obtain B_{aux}=0.18 T for the signal electron with $\tan\theta = p_\perp/p_\parallel = 0$.

Figure 5.5 shows an example of tracks in the curved solenoid spectrometer simu-

lated by a "g4beamline"[1]. A track with desired momentum (105 MeV/c) stays in the same horizontal plane. On the other hand, tracks with wrong momenta (30 MeV/c and 60 MeV/c for example) drift to upward and absorbed by a collimator. Since the vertical drift distance D depends on particle's momentum, unwanted particles can be eliminated by appropriately placing a collimator inside the solenoid as shown in Fig. 5.5.

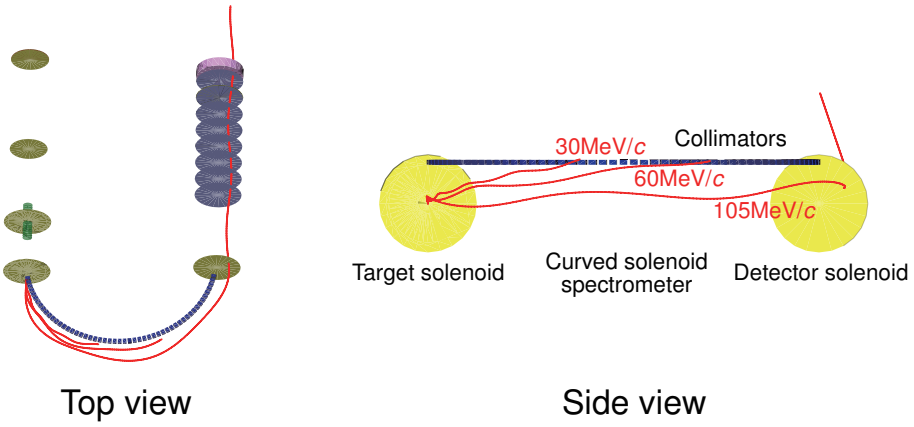

Figure 5.5: Typical tracking events in the electron transport of curved solenoids, simulated by the g4beamline. Electrons of 105 MeV/c, 60 MeV/c and 30 MeV/c are emitted with their tilt angles with respect to the beam axis of 15 degrees at the entrance of the curved solenoid spectrometer.

5.3.2 Electron Transmission Optimization

From the Equation (5.1), drift distance is a function of $p_\perp/p_\parallel$ for given p_{total} and B_0. Since the $p_\perp/p_\parallel$ of electron can be changed by graded magnetic field at the muon-stopping target position, the drift distance is a function of field gradient at the muon-stopping target position. Then, when a particle drifts certain amount to hit the inner wall of the solenoid, that particle will be lost. In short words, the transmission efficiency to the signal electrons and the rejection power to the off-momentum electrons are the functions of both inner radius of the solenoid and the gradient of magnetic field at the muon-stopping target.

In order to optimize the curved solenoid spectrometer, transmission simulations by using g4beamline were performed. In the simulation studies, a bend angle is fixed at 180 degrees, and the solenoidal magnetic field strength is 1 T. A curved collimator was placed along the inside top of the curved solenoid in the region from 0 degree to 180 degrees in a bending angle. The shape of the collimator cross section is rectangular, and dimensions are 5 cm (height) $\times$ 10 cm (width). Electrons were

[1]The g4beamline is a Geant4 based simulation code developed by the MICE experiment (International Muon Ionization Cooling Experiment) at the Rutherford-Appleton laboratory in the UK [41].

generated at the muon-stopping target with various momenta, and the transmission efficiency curve was obtained as a function of electron momentum. Figure 5.6 shows the typical transmission efficiency.

It is clearly seen that the electrons with the momentum below 70∼80 MeV/c are blocked, while the signal electrons (∼100 MeV/c) are transmitted with 30%∼40% of transmission efficiency.

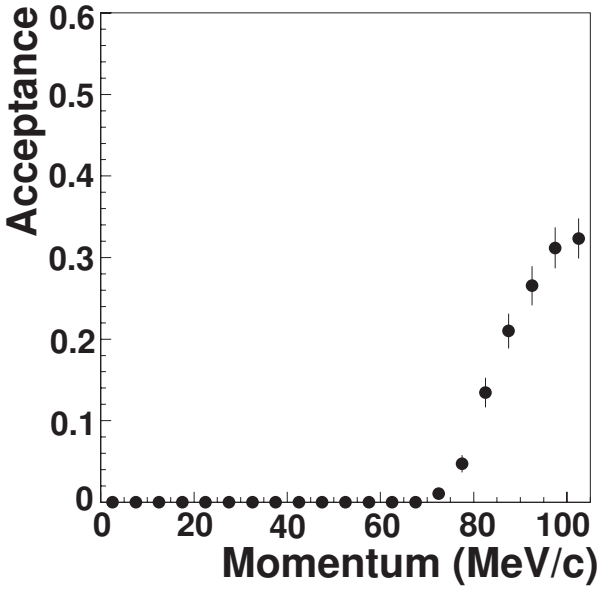

Figure 5.6: Transmission efficiency for electrons from the muon stopping target as a function of momentum. The graded field of 3 T to 1 T is applied to the target region. The inner radius of the spectrometer solenoid is 50 cm.

Fig. 5.7(a) shows a fraction of DIO electrons transmitted through the curved solenoid spectrometer as a function of inner radius for three different setting of the field gradient at the muon-stopping target position. It can be seen that the gradient setting 3T-1T provides the best suppression to the DIO electrons. It is also obvious that the smaller radius gives better suppression. Fig. 5.7(b) shows a fraction of the signal electrons (100 MeV/c) transmitted through the curved solenoid spectrometer. the gradient setting 4T-1T provides the best acceptance, but the difference between 4T-1T and 3T-1T is very small. As the solenoid radius increases, the improvement of the acceptance is modest while the degradation of the DIO suppression is rapid. From these plots, we concluded that the 50 cm of the inner radius and 3T-1T gradient are the optimum.

With these settings, the detector rate is estimated to be of the order of 1 kHz for 10^{11} muons per second in the muon-stopping target. The geometrical acceptance of signal events in a graded magnetic field in the target region is about 0.73, and the transmission efficiency of signal events is about 0.44, thus the overall acceptance of signals of $\mu^- - e^-$ conversion signals is about 0.32.

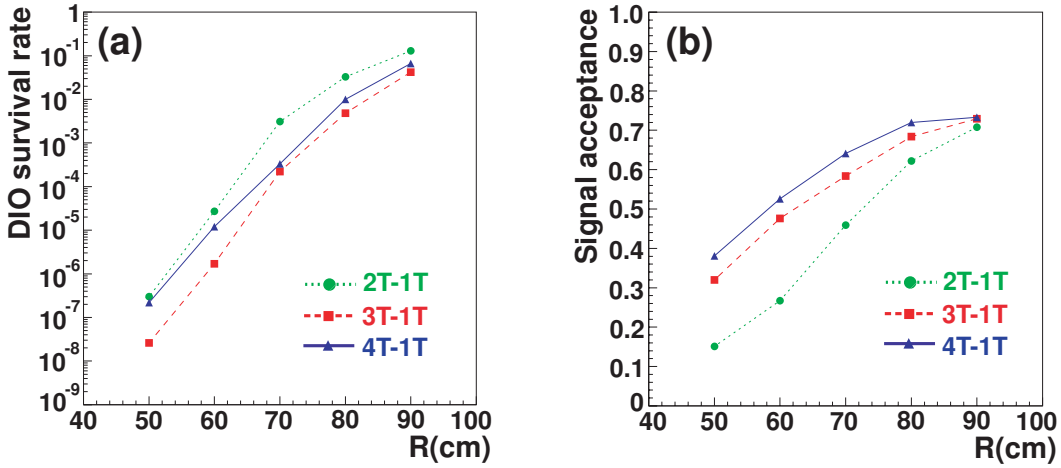

Figure 5.7: (a) Surviving rate of DIO electrons and (b) signal acceptance, as a function of inner radius of the spectrometer solenoid.

5.4 Detection of Electrons

5.4.1 Overview

The main purpose of the electron detector is to distinguish electrons from other particles and to measure their energies, momenta, and timing. The electron detector consists of an electron tracking detector with straw-tube gas chambers for measuring momenta of electrons, an electromagnetic calorimeter for measuring their energies, and fast trigger counters. The detector is placed under a uniform solenoidal magnetic field for momentum tracking. Furthermore, to reduce multiple scattering in momentum measurements, the entire system is placed under vacuum. A candidate layout of the electron detector is shown in Fig.5.8.

Two issues are important when the electron detector is designed. The first issue is single counting rate of the detector. If the counting rate is large, the detector would not be able to distinguish the signal from backgrounds by mistakes in tracking. The second issue is the momentum resolution and that of energy for detected electron. If the resolutions are low, the energy spectrum of $\mu^- - e^-$ conversion will be hidden by that of DIO signals.

5.4.2 Electron Tracking Detector

The required momentum resolution is less than 350 keV/c for a sensitivity of 10^{-16}. Since the momentum of the electrons from $\mu^- - e^-$ conversion is low such as about 105 MeV/c, its intrinsic momentum resolution is dominated by multiple scattering of electrons in the tracker material. Therefore, to reduce a total mass of the tracking detector and to place it in a vacuum are of great importance. For these requirements, a gas wire chamber using straw-tubes, which is strong enough in vacuum, will be used.

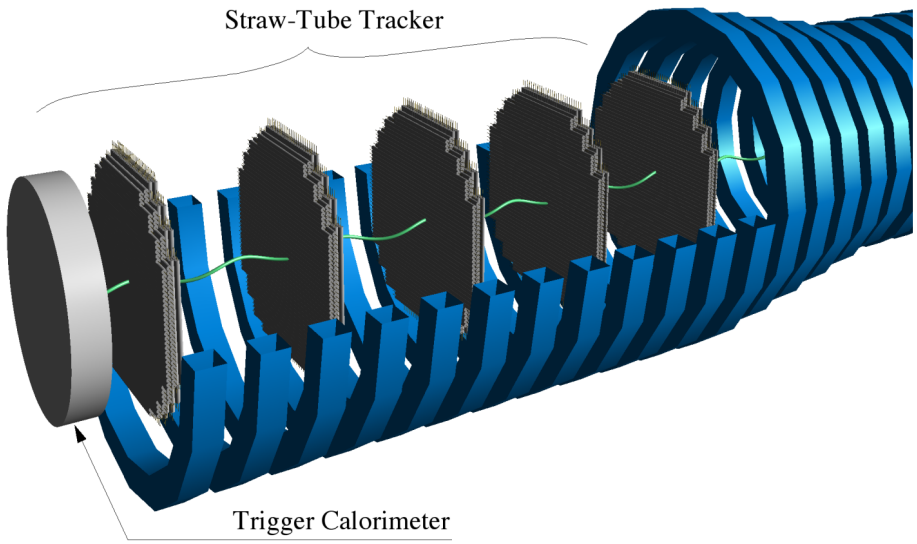

Figure 5.8: Layout of electron detector. It consists of five stations of straw-tube gas chambers, followed by an electron calorimetric detector.

The electron tracking detector consists of five stations of straw-tube gas chambers, where each station is composed of two views (x and y), and one view has two staggered layers of straw-tubes; the distance between each station is 48 cm for all and each of the straw-tubes is 5 mm in diameter and 25 μm in thickness. An anode wire is strung at the center of the straw-tube and is applied high voltage and a gas mixture is filled inside the straw-tube. A radial hit position is determined by a drift time of avalanche charges. A prototype chamber was constructed and was tested to study the performance of the prototype chamber by using a π-beam at KEK. As a result, the position resolution of 100 μm was obtained.

The tracker performance including its momentum resolution and reconstruction efficiency, has been studied by GEANT Monte Carlo simulations. The energy and spatial distribution of electrons from the electron transport system were given by the g4beamline simulation code. With this electron information, helical motions in the tracker region were simulated by GEANT 3. From the simulation with 250 μm position resolution, a momentum resolution of 230 keV/c is obtained. The momentum reconstruction is performed by χ^2 fitting, assuming the helical motion in a uniform magnetic field of 1 T.

To estimate the effect of multiple scattering in the tracker, the genuine momentum resolution was examined without the tracker material, but only with the position resolution of 250 μm. The momentum resolution of 50 keV/c in sigma was achieved. Then, simulation calculation was performed with the tracker materials. Figure 5.9 shows the residual distribution between the reconstructed momentum and true momentum, where the momentum resolution of 203 keV/c in sigma, is obtained. As a result, it is verified that multiple scattering dominate the momentum resolution.

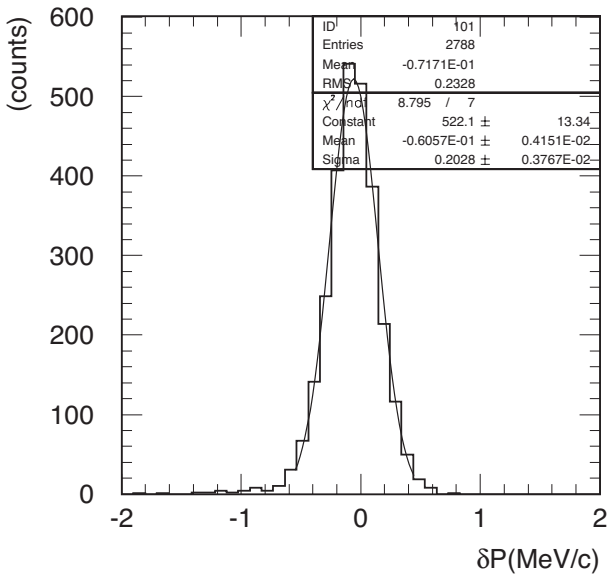

Figure 5.9: Residual distribution between the reconstructed momentum and true momentum.

And the total mass of five-stations-straw chambers is small enough to achieve the momentum resolution of 230 keV/c, which meets the requirements of less than 350 keV/c.

The contamination of DIO background into the signal region is estimated by using the events with χ^2 cut, where χ^2 less than 9.0 is selected so as to achieve the momentum resolution of 350 keV/c. As a results, the contamination is estimated as 0.05 events after the momentum reconstruction. Therefore, the DIO background by the momentum miss-reconstruction is confirmed to be negligible.

The momentum resolution of 350 keV/c is required to identify the conversion signal from DIO background. The requirement is achieved by the tracking detector using straw-tube chambers. However, DIO background may contaminate into the signal region by miss-reconstruction of the momentum, although the χ^2 function has good value. Therefore, the relation between the momentum resolution and the value of the χ^2 function is shown in Fig. 5.10. From this figure, it is confirmed that the value of the χ^2 function reflects the goodness of the tracking.

5.4.3 Electron Calorimeter

The electron calorimeter, which is located downstream from the tracking detector, would serve three purposes. One is to measure the energy of electrons. High energy resolution is required. The second is to provide a timing signal for the electron events, and at the same time give a trigger signal which could be used to select events to be recorded for further analysis. In this regard, fast response and high efficiency are needed. The third is to provide additional data on hit positions of the electron tracks at the calorimeter location. This would be useful in eliminating false tracking.

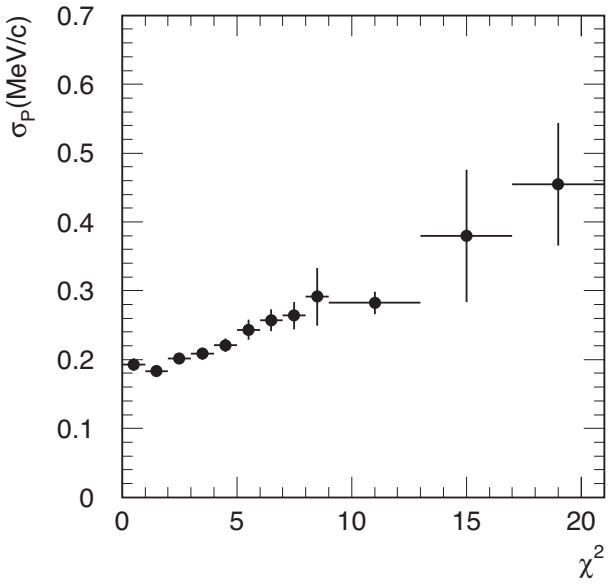

Figure 5.10: Momentum resolution and the value of χ^2 function for the conversion electrons. Events which have $\chi^2 < 9$ are selected.

Redundant measurements of energy and momentum of electrons are of critical importance to identify the $\mu^- - e^-$ conversion signal events from backgrounds. On this regards, the energy resolution must be very good, and it should have large light yields. Also to reduce a hit overlapped to others, smaller Moliére radius is needed. In addition, fast time response with fast decay constant (< 100 nsec) is required.

Candidate inorganic crystals, such as cerium-doped Gd_2SiO_5 (GSO) crystals, have been considered. A GSO crystal have a large light yield and a small decay constant, comparing other crystals as shown in Table 5.3. Therefore, GSO crystal is a suitable scintillator for the calorimeter.

Table 5.3: The characteristics of inorganic scintillator crystals.

	GSO(Ce)	BGO	PWO	BaF_2	CsI(Tl)
Density (g/cm^3)	6.71	7.13	8.2	4.89	4.51
Radiation length (cm)	1.38	1.11	0.92	2.03	1.85
Decay constant (ns)	30-60	300	3	630	1,300
Wavelength (nm)	430	480	430	300	560
Light yield (NaI(Tl)=100)	20	7-10	0.26	21	45
Refraction index	1.85	2.15	2.2	1.50	1.79

Segmentation is desired to reduce spatial overlapping. The segmentation would also give an additional hit position which would help reconstruction of the tracks. By comparing the energy (which is measured at the trigger/energy detector) and the momentum (which is measured at the tracking detector) of the tracks, the particle

can be identified. The calorimeter consists of GSO cells with 3×3 cm^2 cross section and 11 radiation lengths long (about 15 cm for GSO). If the calorimeter covers the cross section of the detector region (7850 cm^2), about 900 GSO cells will be used. Since that depends on the magnetic field in the detector region and geometry of the calorimeter, it will be optimized by further R&D.

The photon readout from the crystals is one of the key elements for construction of the calorimeter. The electron calorimeter is located in vacuum to suppress the multiple scattering in the air. Therefore, low power device must be used for photon readout instead of photo-multiplier. One possible candidate is an avalanche photo-diode (APD).

5.5 Cosmic-Ray Shield

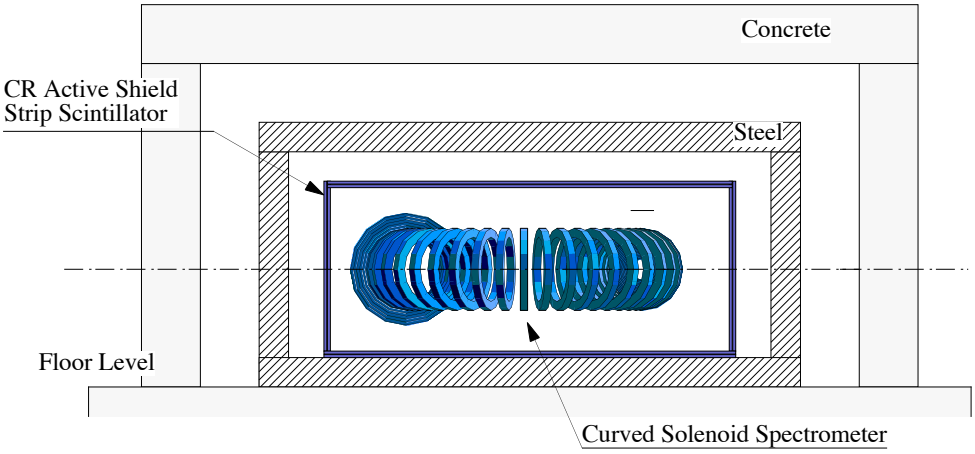

Figure 5.11: Schematic view of cosmic-ray shield.

Cosmic-ray-induced electrons (or other particles misidentified as electrons) may cause background events. Therefore, passive and active shielding against cosmic rays covering the entirety of detector is considered. Figure 5.11 shows a preliminary layout of the cosmic ray shield. The concrete has a thickness of 1 meters. The passive shielding consists of a combination of steel and concrete wall. The steel enclosure shown in Fig. 5.11 provides a return path for the detector magnetic field, as well as a passive extra shield against cosmic rays. Steel enclosure has a wall thickness of about 0.5 meters. It is useful to reject low energy muons and electrons from muon decays outside the experimental apparatus. The active shielding will be placed inside the passive shielding, and it covers the whole electron detector, namely the muon stopping target, the electron transport of curved solenoids and the detector solenoids. The candidate design of the active shielding is two layers of scintillator strips. If the efficiency of each scintillator strip layer to be 99 %, the rejection performance of the cosmic-ray background will be 10^{-4}.

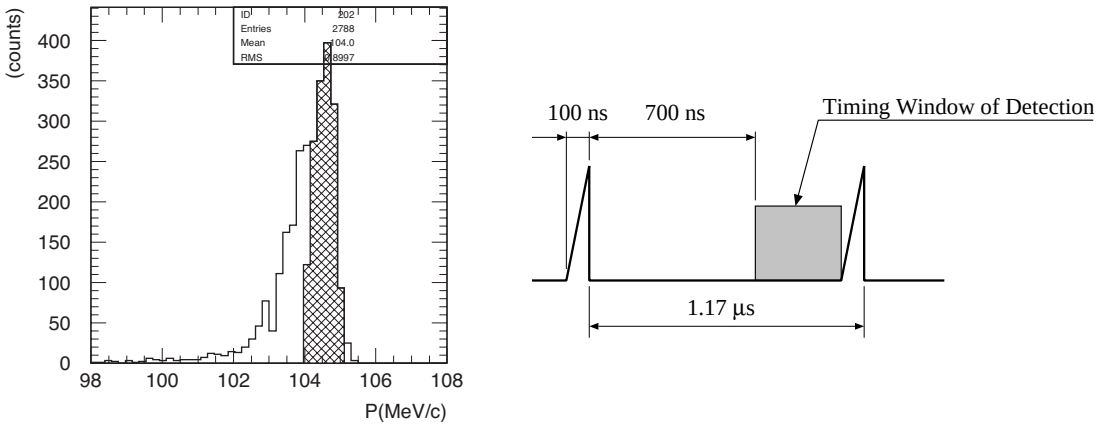

Figure 5.12: (Left) Reconstructed momentum distribution of 105 MeV electrons. This is not corrected for average energy loss of electrons (of about 0.4 MeV/c). The hatched region is the energy region for the signal, which is set to that from 104.0 MeV/c to 105.2 MeV/c for an uncorrected energy scale. (Right) Timing window of detection.

5.6 Acceptance

The acceptance is determined by the geometrical acceptance, which has been discussed before, and the analysis acceptance given by the analysis cuts. They are discussed in the following.

- *Transverse Momentum :*
  To eliminate background events, such as those from beam electrons and muon decay in flight, a transverse momentum of electrons greater than 52 MeV/c ($p_t > 52$ MeV/c) at the detector position is desired.

- χ^2 *:*
  The contamination of DIO background into the signal region is estimated by using the events with χ^2 cut, where χ^2 less than 9.0 is selected so as to achieve the momentum resolution of 350 keV/c.

Table 5.4: Summary of signal acceptance.

	Acceptance
Geometrical Acceptance	0.73
Electron Transport Efficiency	0.44
Transverse Momentum ($p_t > 52$ MeV/c)	0.67
χ^2 Cut ($\chi^2 < 9$)	0.86
Energy Selection	0.56
Timing Window of Detection	0.38
Total	0.04

- *Energy :*
  To determine the energy region for the $\mu^- - e^-$ conversion signals, the $\mu^- - e^-$ conversion electrons were generated inside the muon-stopping target, and reconstructed using a tracking program. Figure 5.12 shows the distribution of the reconstructed momentum (without correction for energy loss in the target), where a momentum spread of about 350 keV/c is seen. The signal region is determined to be 104.0 MeV/c to 105.2 MeV/c, which corresponds to one 1.7 sigma width of momentum spread. In this signal region, about 56% of total signal events is contained.
- *Timing :*
  Measurement starts about 700 nsec after the prompt to avoid beam-related prompt background events. A schematic timing chart is shown in Fig. 5.12. The acceptance in the detection window is about 0.38 for aluminum.

Table 5.4 summarizes the acceptances. The total signal acceptance for spectrometer and detector is 0.04.

Chapter 6

Sensitivity and Background

6.1 Signal Sensitivity

We estimate the signal sensitivity of our search for $\mu^- - e^-$ conversion. The single event sensitivity is defined by the number of muons stopping in the muon target (N_μ), the fraction of captured muons (f_{cap}), and the detector acceptance (A_e), as follows.

$$B(\mu^- + \mathrm{Al} \to e^- + \mathrm{Al}) \sim \frac{1}{N_\mu \cdot f_{cap} \cdot A_e} \tag{6.1}$$

The total number of muons which are stopped in the muon-stopping target (N_μ) of about 1.1×10^{18} for 4×10^7 sec is estimated as shown in Table 6.1.[1] For aluminum, the fraction of muons captured is about $f_{cap} = 0.6$. The acceptance A_e is summarized as shown in Table 5.4. The total acceptance for the signal is 0.04. By using N_μ, f_{cap}

Table 6.1: Total number of muons delivered to the muon-stopping target.

Proton intensity	4×10^{13} protons/sec
Running time	4×10^7 sec
Rate of muons per proton transported to the target	0.0024
Muon Stopping Efficiency	0.29
Total	1.1×10^{18} stopped muons

and A_e, the single event sensitivity is obtained by

$$B(\mu^- + \mathrm{Al} \to e^- + \mathrm{Al}) = \frac{1}{1.1 \times 10^{18} \times 0.6 \times 0.04} = 4 \times 10^{-17}. \tag{6.2}$$

Since a 90% confidence level (CL) upper limit is given by $2.3/(N_\mu \cdot f_{cap} \cdot A_e)$, the upper limit is obtained as

$$B(\mu^- + \mathrm{Al} \to e^- + \mathrm{Al}) < 10^{-16} \quad (90\%\ \mathrm{C.L.}), \tag{6.3}$$

[1] If a proton target of heavy materials such as tungsten can be used, the pion production yield would increase by a factor of two, and thereby the rate of muons per proton would be 0.0048 and a running time would be reduced to 2×10^7 sec.

which is about $10,000$ times better than the current published limit obtained by SINDRUM II at PSI of $< 7 \times 10^{-13}$ (90% C.L.) [6].

6.2 Background Events and Their Rejection

Potential sources of background events for $\mu^- - e^-$ conversion are categorized into three different types. They are

1. Intrinsic physics background events:
   Intrinsic physics background events originate mostly from muons stopping in the muon-stopping target. They arise from muon decays in orbit, radiative muon capture, and particle emission after muon capture.
2. Beam-related background events:
   This type of background event is caused by particles in a beam, such as electrons, pions, muons, and antiprotons. There are two different types, one is a prompt background event and the other is a late-arriving background event. For the former, beam pulsing with a high beam extinction is a very effective way of rejecting the background events.
3. Cosmic-ray background events:

The rejection techniques and the estimations to the remaining backgrounds are discussed in details below.

6.2.1 Intrinsic Physics Backgrounds

6.2.1.1 Muon Decay in Orbit

When muonic atoms are formed, muons mostly come to its ground state before decaying. Then, they either get captured by a nucleus with emitting a neutrino (nuclear muon capture) or decay in orbit (DIO). For instance, for an aluminum target, about 40 % of muons decay in orbit. The electrons from muon decay in orbit become one of the serious background sources. Their energy spectrum in the energy region lower than 50 MeV mostly resembles the Michel spectrum of ordinary muon decays. However, due to nuclear recoils, a high energy tail exists and extends up to the energy region of interest for the signal events. One of the way to distinguish the signal events from DIO electrons is to measure the energy of electrons as precisely as possible. As will be discussed below, since the energy spectrum falls sharply as $(E_{\mu e} - E_e)^5$ where $E_{\mu e}$ and E_e are the energy of $\mu^- - e^-$ conversion signal and the energy of electrons respectively, modest detection resolution would be sufficient for their separation.

The energy spectra of DIO electrons are studied with nuclear recoil-energy taken into account [42, 43]. With the approximation of a constant nuclear-recoil energy, the electron spectrum with an expansion in powers of the electron energy (E_e) at the end-point energy is given by

$$N(E_e)dE_e = \left(\frac{E_e}{m_\mu}\right)^2 \left(\frac{\delta_1}{m_\mu}\right)^5 \left[D + E \cdot \left(\frac{\delta_1}{m_\mu}\right) + F \cdot \left(\frac{\delta}{m_\mu}\right)\right] dE_e, \qquad (6.4)$$

where $\delta = E_{\mu e} - E_e$ and $\delta_1 = E_{\mu e} - E_e - E_{\rm rec}$, where $E_{\rm rec}$ is the nuclear-recoil energy given by $E_{\rm rec} = E_e^2/(2M_A)$. The coefficients D, E and F as well as the end-point energy are calculated as shown in Table 6.2 [25, 38]. It should be stressed that the spectrum falls off sharply as the fifth power of δ_1 towards its end-point, $(\delta_1)^5 \approx (E_{\mu e} - E_e)^5$.

Table 6.2: Numerical values of D, E, F and the energy of $\mu^- - e^-$ conversion electrons.

Z	$D(\times 10^{21})$	$E(\times 10^{21})$	$F(\times 10^{21})$	$E_{\mu e}$ (MeV)
13	0.36	0.95	2.27	105.0
22	2.04	6.21	13.28	104.2

In order to evaluate the background contribution from DIO electrons, their rates and energy spectra have been studied. Since Eq.(6.4) is valid only near the endpoint of the spectrum, the numerical values of the spectrum shapes of DIO electrons complied by Watanabe et al. [26] was used for the low energy region. Both spectra are connected smoothly at $E_e = 100$ MeV. After that, This theoretical spectrum was convoluted with the Monte Carlo studied response function of the electron tracker (Fig. 5.12), that includes detector resolution, multiple scattering effect and analysis errors. Figure 6.1 shows the expected electron momentum spectra for both signal electrons and DIO electrons. The number of DIO events sneaking into the signal fiducial region (104.0$\sim$105.2 MeV/c) was estimated to be less than 0.05 events.

6.2.1.2 Radiative Muon Capture

Radiative muon capture (RMC), $\mu^- + (A, Z) \rightarrow \nu_\mu + (A, Z-1) + \gamma$, followed by asymmetric e^+e^- conversion of the photon, is another source of intrinsic background events. In an aluminum target, it is $\mu^- + Al \rightarrow \nu_\mu + Mg + \gamma$, where the endpoint of photon energy is 102.5 MeV. The probability per muon capture of producing a photon with energy exceeding 100.5 MeV is about 4×10^{-9} [38]. The conversion probability of photon in the target is about 0.005, and the probability that the energy of the electron produced photon conversion exceeds 100 MeV is about 0.005. Thus, The probability of producing an electron above 100 MeV is about 10^{-13}. These electrons are all less than 102 MeV. Since the signal region from 104.3 MeV to 105.0 MeV is determined, the probability for those events to come in to the signal region is estimated by integrating high energy tail of the resolution function of the tracking system. The probability is evaluated to be less than 10^{-6}. From those, the background rate from RMC is about < 0.001 at the signal sensitivity of 10^{-16}. The background of this type cannot be separated, but the measured energy spectrum of electrons can be fitted into a combination of DIO and RMC to estimate each contribution.

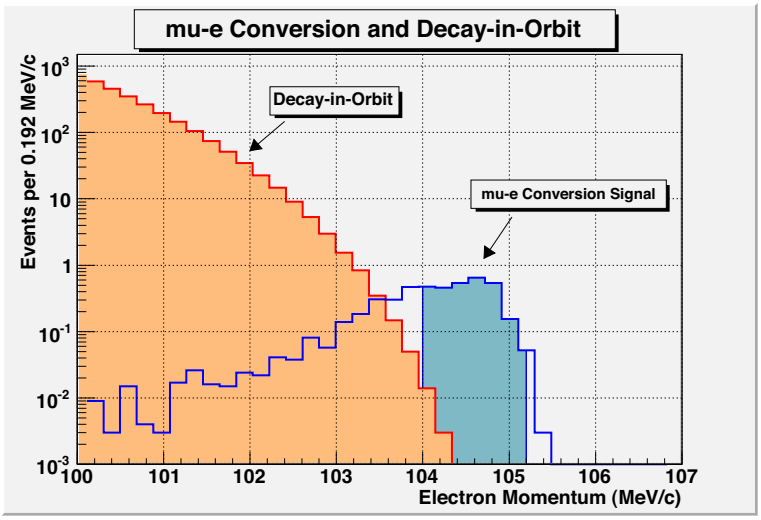

Figure 6.1: Electron momentum spectra of μ-e conversion signal and Decay-in-Orbit (DIO) background from a muonic atom in aluminum. DIO spectrum is obtained by convoluting a theoretical DIO spectrum shape with simulated detector response. The vertical axis is a number of events for 1.1×10^{18} stopped muons. The branching ratio is assumed to be 10^{-16} for μ-e conversion spectrum. The horizontal axis is electron momentum with energy loss in the target uncorrected.

6.2.1.3 Muon Capture with Neutron Emission

When a negative muon is stopped in matter, it is captured in an atomic orbit. It then cascades to the 1s level where it either decays or is captured by the nucleus. As a result of the weak interaction, the latter possibility leads to the following nuclear reaction.

$$\mu^- + N(A, Z) \rightarrow \nu_\mu + N^*(A, Z-1). \tag{6.5}$$

Most of the energy released (≈100 MeV) is carried away by the neutrino. The mean excitation energy of N^* is around 15 to 20 MeV. Thus, N^* can de-excite by emitting one or more neutrons, or charged particles, or it may de-excite via the ordinary electromagnetic mode. They may generate background electrons by the interaction with muon stopping target, solenoid material and so on.

The dominant reaction is neutron emission.

$$\mu^- + N(A, Z) \rightarrow \nu_\mu + xn + N(A-x, Z-1), \tag{6.6}$$

with $x \geq 1$. With the electromagnetic de-excitation mode ($x = 0$), these reaction channels account for more than 95% of the total reaction probability.

The inclusive energy spectrum for neutrons emitted after muon capture for Si and Ca is shown in Fig. 6.2, which is measured in Ref. [44]. They are consistent with an exponential dependence on the neutron energy given by the expression of $P(E) = \exp(-\alpha E_n + \beta)$. The fitting results for Si and Ca are summarized in Table

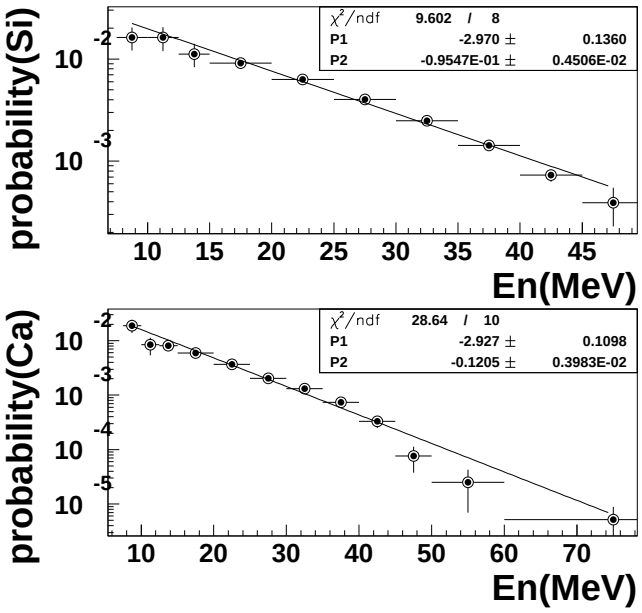

Figure 6.2: Probability of muon capture with a neutron as a function of neutron kinetic energy (E_n) for Si and Ca.

Table 6.3: The probability of muon capture with neutrons emission for Si and Ca by the expression of $P(E) = \exp(-\alpha E_n + \beta)$.

	α	β
Si	$-0.096\pm$	-2.970 ± 0.136
Ca	-0.121 ± 0.004	-2.927 ± 0.110

6.3. Since the probability is not much different for materials, the values of Si are used for aluminum.

Background electrons generated by neutrons from muon capture are estimated by GEANT 3 simulation. In this simulation, GCALOR is used as a hadron package. The estimated background contamination into the signal region is less than 0.001.

6.2.1.4 Muon Capture with Emission of Charged Particles

For much less probability than neutron emission, there are reaction channels involving the emission of protons and α-particles.

$$\mu^- + N(A, Z) \rightarrow \nu_\mu + p + xn + N(A - x - 1, Z - 2), \tag{6.7}$$

$$\mu^- + N(A, Z) \rightarrow \nu_\mu + \alpha + N(A - 4, Z - 3). \tag{6.8}$$

Table 6.4: The probability of muon capture with outgoing charged particles as a function of $\exp(\alpha V + \beta)$, where V is the Coulomb barrier. The probability for Al and Ti is also shown.

Reaction	α	β	Al	Ti
$P(p)$	-0.379 ± 0.017	-3.631 ± 0.187	5.2×10^{-3}	2.5×10^{-3}
$P(pn)$	-0.371 ± 0.022	-1.910 ± 0.186	3.0×10^{-2}	1.5×10^{-2}
$P(p2n)$	-0.383 ± 0.024	-2.104 ± 0.211	2.3×10^{-2}	1.1×10^{-2}
$P(p3n)$	-0.338 ± 0.121	-2.504 ± 1.141	1.9×10^{-2}	1.0×10^{-2}
$P(\alpha)$	-0.460 ± 0.030	-2.203 ± 0.267	7.0×10^{-3}	1.5×10^{-3}

where (A, Z) is a nucleus with a mass number of A and an atomic number Z. From the cross section table in Ref. [45], the partial reaction probability of muon capture with charged particles is plotted against the Coulomb barrier. The classical Coulomb barrier V is calculated as

$$V = \frac{zZ'e^2}{r_0 A^{1/3} + \rho} \tag{6.9}$$

$$V[\mathrm{MeV}] = \frac{zZ}{r_0[\mathrm{fm}]A^{1/3} + \rho[\mathrm{fm}]} \frac{197.3}{137.0} \tag{6.10}$$

where z and Z' are the charges of the outgoing particles and of the residual nucleus, respectively. r_0 is taken as 1.35 fm, and ρ as 0 fm for protons and 1.2 fm for α-particles. For example, V for aluminum is calculated as 5.4 MeV and 7.2 MeV for protons and α-particles, respectively. The probability of muon capture with outgoing charged particles is expressed an exponential function of the Coulomb barrier, and the results are summarized in Table 6.4. In Table 6.4, the probability for aluminum and titanium is also shown.

The kinetic energy spectrum of the outgoing charged particles is expressed as

$$P(E_c) = P_0 \exp(-E_c/E_0), \tag{6.11}$$

where P_0 is a normalization constant and E_c is the kinetic energy spectrum of the outgoing charged particles and E_0 is a parameter to determine shape of the spectrum distribution [46]. The E_0 is expressed as a function of Z, which is shown in [46] as a table. Fitting by a linear function, E_0 is determined as,

$$E_0 = 0.03614 \cdot Z + 7.103. \tag{6.12}$$

For aluminum (Z=13), E_0 is obtained as 7.6 MeV.

Background electrons by charged particles from muon capture are estimated by GEANT 3 simulation. In this simulation, GCALOR is used as the hadron package. The background is estimated to be less than 0.001.

6.2.2 Beam-related Backgrounds

6.2.2.1 Radiative Pion Capture

When pions stop in materials, they are immediately captured by a nucleus. About 2 % of the pion captures are associated with emitting photons. It is called radiative pion capture (RPC), $\pi^- + (A, Z) \rightarrow (A, Z-1) + \gamma$. Radiative pion capture followed by internal and external asymmetric e^+e^- conversion of the photon ($\gamma \rightarrow e^+e^-$) would become one of the most serious source of the background. The RPC background can be roughly estimated by the following equation.

$$N_{\rm RPC} = N_{\rm p} \cdot R_{\pi/{\rm p}} \cdot P_{\pi-{\rm surv}} \cdot R_{\rm ext} \cdot P_{\gamma} \cdot R_{\rm accept}. \tag{6.13}$$

where $N_{\rm p}$ is a number of delivered protons, and $R_{\pi/{\rm p}}$ is a number of pions entering transport solenoid per one proton hitting the production target. $P_{\pi-{\rm surv}}$ is pion survival probability in the transport solenoid. P_{γ} is probability of photon conversion in the Al target with a conversion electron in a signal region from 104.0 to 105.2 MeV. $R_{\rm accept}$ is an acceptance for signal without a timing-window factor. $R_{\rm ext}$ is the proton extinction at the off-beam timing.

In this experiment, $N_{\rm p}$ is 16×10^{20}, and $R_{\pi/{\rm p}}$ is about 1.5×10^{-2} at 8 GeV operation. All the charge particles should travel the transport solenoid of about 50 m long. Since the momentum is selected to be about 70 MeV/c in the curved solenoid, pions take at least 350 ns to go through the transport solenoid. Therefore, $P_{\pi-{\rm surv}}$ is about 1.5×10^{-6}. P_{γ} is less than 3.5×10^{-5}, according to GEANT 3 simulations. $R_{\rm accept}$ is 0.10 and $R_{\rm ext}$ is assumed as 10^{-9}. As a result, the estimated background rate at sensitivity of 10^{-16} is about 0.12 events.

The second contribution to RPC comes from late-arriving pions which take a very long time to traverse and arrive at the muon-stopping target very late. For those events, the proton extinction does not apply for the rejection. However, since the detection window starts about 700 nsec after the proton pulse, those pions live long, of about 700 nsec. The surviving probability for those late arriving pions per proton of 0.4×10^{-17} which should be substituted for the product of ($P_{\pi-{\rm surv}} \cdot R_{\rm ext}$) in Eq.(6.13). As a result, the expected of RPC background of this type is about 0.002 events. This type of background is easily monitored. By measuring a number of energetic electrons as a function of time during the pulse, the detection window can be appropriately examined.

6.2.2.2 Muon Decay in Flight

Muons decaying in flight can produce energetic electrons that have sufficient total momentum (of about $p_{\rm total} > 102$ MeV/c) and transverse momentum (of about $p_t > 52$ MeV/c). For the decay electrons to have $p_{\rm total} > 102$ MeV/c, the muon momentum must exceed 77 MeV/c ($p_{\mu} > 77$ MeV/c). A Monte Carlo simulation has been done to estimate the yield of muons of $p_{\mu} > 77$ MeV/c transported through the muon beam line, and it is about 2×10^{-4} per incident proton. The probability for muons to decay in flight in the muon beam line is about 3×10^{-2}. And the probability having an electron energy of 103 MeV/$c < p_{total} <$ 105 MeV/c, and $p_t > 52$ MeV/c is less

than 10^{-8}. With the beam extinction of 10^{-9}, the total background level from muon decay in flight is less than 0.02.

6.2.2.3 Pion Decay in Flight

Beam pions decaying to electrons ($\pi \rightarrow e + \nu$) are also a potential source of background. The π momentum must exceed 60 MeV/c to make this background process. A GEANT 3 Monte Carlo simulation was done to estimate the probability of pions with $p_\pi > 60$ MeV/c passing though the muon beam line solenoids. It is noted that the muon beam line has capability to transport beam particles whose momentum is less than about 80 MeV/c. The probability is about 5×10^{-6}. The branching ratio of $\pi \rightarrow e+\nu$ is about 1.0×10^{-4}. The probability of the decay electron from $\pi \rightarrow e+\nu$ to have $E_e > 102$ MeV and $p_t > 52$ MeV/c is about 5×10^{-6}. With the beam extinction factor of 10^{-9}, the background level from pion decay in flight is less than 10^{-3}.

6.2.2.4 Beam Electrons

If electrons in a beam are scattered at the muon stopping target into the detector, they might become background events. The muon beam line is designed to pass beam particles whose momentum is less than 80 MeV/c. By using a GEANT 3 Monte Carlo simulation, the probability of beam particles of 100 MeV/c being transported through this beam line is less than 10^{-8} (statistically limited). Then, the probability for electrons of about 100 MeV in energy from the muon beam line to be scattered off in the target and have a transverse momentum exceeding 52 MeV/c is about 5×10^{-6} per proton. With 16×10^{20} protons and the beam extinction of 10^{-9}, the expected background rate of beam electrons is 0.08.

6.2.2.5 Neutron Induced Background

Background induced by neutrons in a beam with high kinetic energy coming through the muon beam line is estimated. Those neutrons could pass through the muon beam line by being kept reflecting its inner sides. The neutrons which can produce electrons of 100 MeV must exceed its kinetic energy of 100 MeV. The rate and energy distribution of neutrons whose kinetic energy is more than 100 MeV/c were examined by MARS simulations. It is about 3×10^{-7} neutrons/proton. And by using GEANT 3 Monte Carlo simulation, an average transit time of those neutrons arriving at the muon stopping target is estimated and it is about 300 nsec, and much less than the waiting time of 700 nsec before detection window opens. Therefore, it is regarded as a prompt background. By using GEANT 3 Monte Carlo simulation, the probability for those neutrons to produce electrons of about 100 MeV in energy was estimated and found to be about 10^{-7}. With the beam extinction of 10^{-9}, the background rate of neutron induced of this type is about 0.024.

6.2.2.6 Antiproton Induced Background

Another potential source of background is induced by antiprotons. Owing to the momentum selection of the muon beam line consisting of curved transport solenoids, only antiprotons of low momentum (say, less than 80 MeV/c) can pass the muon beam line. These antiprotons have very low kinetic energy and velocity. Therefore, they are not suppressed by the beam extinction. There are several ways to suppress antiproton induced backgrounds. They are

- reduction of the production rates of antiprotons by decreasing proton beam energy, and
- absorption in a thin absorber material placed in the muon beam line.

Here, the antiproton induced background is sensitive to the incident proton energy. When the incident proton energy is lower, the production of antiprotons is less. The current choice of a proton energy of 8 GeV is chosen to reduce the production rate of antiprotons. The first curved section of the muon transport beam line would eliminate antiprotons of high energy. Then, a thin foil of beryllium of 120 μm thickness is placed in the middle section of the beam line to absorb those of low energy.

The production yields of antiprotons for various proton energies are studied by MARS. Also, the energy and angular distributions are modeled based on those of pions. The antiprotons are transported down in the muon beam line in GEANT 3 Monte Carlo simulations. Also based on the MECO experiment [38], expected numbers of electrons and pions in the detector from antiprotons annihilation were studied by using annihilation cross sections experimentally determined. These annihilation products were then tracked with GEANT, and the number of particle fluxes coming to the muon stopping target was calculated. The result shows that primary background resulted from radiative pion capture, and second contribution resulted from electrons scattering in the muon stopping target. Table 6.5 summarizes the results of antiproton induced background [38]. From Table 6.5, the rate of antiproton induced background is about 0.007 at sensitivity of 10^{-16}.

Table 6.5: Antiprotons induced backgrounds for different incident proton momenta.

proton momentum (GeV/c)	number of $\bar{p}/p$ produced	number of $\bar{p}/p$ entering transport	background events
5	3.9×10^{-10}	7.4×10^{-15}	7×10^{-7}
6	5.3×10^{-8}	8.0×10^{-13}	8×10^{-5}
7	1.4×10^{-6}	1.2×10^{-11}	1.2×10^{-3}
8	8.5×10^{-6}	6.8×10^{-11}	7×10^{-3}

6.2.3 Cosmic Ray Induced Background

Cosmic ray-induced electron backgrounds are potentially an important background. To reduce this type of backgrounds, active and passive shielding are needed. A passive shielding of 2 meter concrete and 0.5 m of steel might be necessary. Layers of scintillator veto counters surrounding the detector with combined efficiency for charged particle detection of 99.99 % (1 % of inefficiency per layer) are required. In off-line analysis, event selection of eliminating extra particles in the tracking system or in the calorimeter in coincidence with the electron signal might be considered.

The cosmic-ray induced background is estimated by GEANT 3 Monte Carlo simulations. The energy and angular distributions of cosmic rays are determined based on the known parameters. Namely, the energy spectrum at a sea level is essentially flat below 1 GeV, and the flux follows with a power law approximately given by $E^{-2.5}$, with E in GeV. The angular distribution is approximated by $dN/d\theta \sim e^{-1.43\theta}$. The muon flux is about 60 % of positives and 40 % of negatives. Since electrons and muons can be identified by the energy measurement by the calorimeter, electrons from muon decay, δ-ray and pair production become potential backgrounds. By GEANT 3 Monte Carlo simulations, the expected level of cosmic ray-induced backgrounds is less than 0.2 events for 4×10^7 seconds of running with a beam duty factor of about 0.5. If the duty factor is reduced down to less than 0.1 by shortening the slow-extraction time of the primary proton beam, the expected cosmic-ray backgrounds will be less than 0.04 events.

6.2.4 Summary of Background Rates

The expected background rates at a sensitivity of 10^{-16} are summarized in Table 6.6.

Table 6.6: Summary of the background rates at a sensitivity of 10^{-16}. Backgrounds identified with an asterisk are proportional to the beam extinction, and the rates in the table assume 10^{-9} beam extinction.

Background	Events	Comments
Muon decay in orbit	0.05	230 keV (sigma) assumed
Pattern recognition errors	<0.001	
Radiative muon capture	<0.001	
Muon capture with neutron emission	<0.001	
Muon capture with charged particle emission	<0.001	
Radiative pion capture*	0.12	prompt pions
Radiative pion capture	0.002	due to late arriving pions
Muon decay in flight*	< 0.02	
Pion decay in flight*	< 0.001	
Beam electrons*	0.08	
Neutron induced*	0.024	for high energy neutrons
Antiproton induced	0.007	for 8 GeV protons
Cosmic rays induced	0.2	with 10^{-4} veto inefficiency
Total	0.50	

Chapter 7

Experimental Layout at J-PARC

7.1 Overview

The experimental layout for the case when the experimental setup for $\mu^- - e^-$ conversion is installed at J-PARC is described in this chapter. The experimental setup should be located in the J-PARC Nuclear and Particle (NP) Hall, which is **the only experimental hall where a proton beam from slow-extraction is delivered**. The NP Hall is under construction now (as winter, 2007), and some experiments have already been officially approved and allocated to the experimental hall. Since our proposal of carrying the experiment out at the NP hall comes later than the others, at this moment, **no definite location and experimental layout for the proposed experiment have been determined.**

7.2 Layout Issues

Several considerations have to be taken into account in order to accommodate the experiment in the NP experimental hall. Some of them are listed in the following.

- A new target station,
  A new target station for this experiment (in addition to the current T1 target) is needed because a proton target should be surrounded by superconducting solenoid magnets for pion capture. It should be noted that a new target station is only for a beam power of 56 kW.

- Proton beam optics,
  Beam optics to focus protons of 8 GeV to the proton target must be made. Particular care has to be paid for a room to install the external extinction devices and monitors in the proton beam line before the proton target. Effects of proton beam halo to the superconducting solenoids should be minimized, as well as those from radiation from the beam dump. It might be not necessary to defocus the primary proton beam since the beam power is only 56 kW for this experiment.

- Radiation shielding,
  Shielding for the beam line and target is needed towards top, bottom (floor) and sides (in particular downstream-side). We have calculated that shielding blocks equivalent to about 7 meter thick concrete might be needed. Detailed calculations of radiation shielding requirements will be done

- Minimization of interference with the other experimental areas,

To fulfill the above considerations, some modifications of the infrastructure in the NP Hall might be needed.

7.3 Examples of Layouts

There might be two potential layouts that could be considered. One of them is to use the existing A-Line. In this case, the present beam dump is moved towards the downstream direction, and a proton beam is bent at the region near the T2 target location, as shown in Fig.7.1. The reason why the proton beam is bent from the original A-Line is to eliminate radiation from the T1 target, when it is in a beam, towards the superconducting solenoid magnets for pion capture, based on the running scenario when the experiments with the T1 target and the proposal experiment can run alternatively. When the proposed experiment is not running, the bending magnet is turned off and a proton beam with full beam power can be safely bypassed from the proposed experiment setup and is brought to the full power beam dump. In this bent proton beam line, a new dedicated beam dump would be needed. It is not necessary to be a full beam power dump since only a proton beam power of 7 μA with 8 GeV (which is 56 kW, about 1/8 of the full beam power) is needed. Also the proton target is only for 56 kW.

The second layout is to use the B-line, as shown in Fig.7.2. The proton target can be located at the 2nd beam split of the B-line. The detector will be located at the K1.1BR area. There might be some conflict with other experiments with the experiment users of the K1.1BR area and the B-line. However, it should be solved by coordination of time scheduling because as shown in the next chapter, the earliest year for the proposed experiment to run might be the year of 2012. One of the advantages of this layout is a total cost of the experiment might be cheaper since it is not necessary to move the present beam dump.

These experimental layouts shown in the above are some of examples. They need more careful considerations and consultation with the KEK beam-channel group. They are not exclusive, and if there are any better layouts and solutions, we can consider those for the proposed experiment.

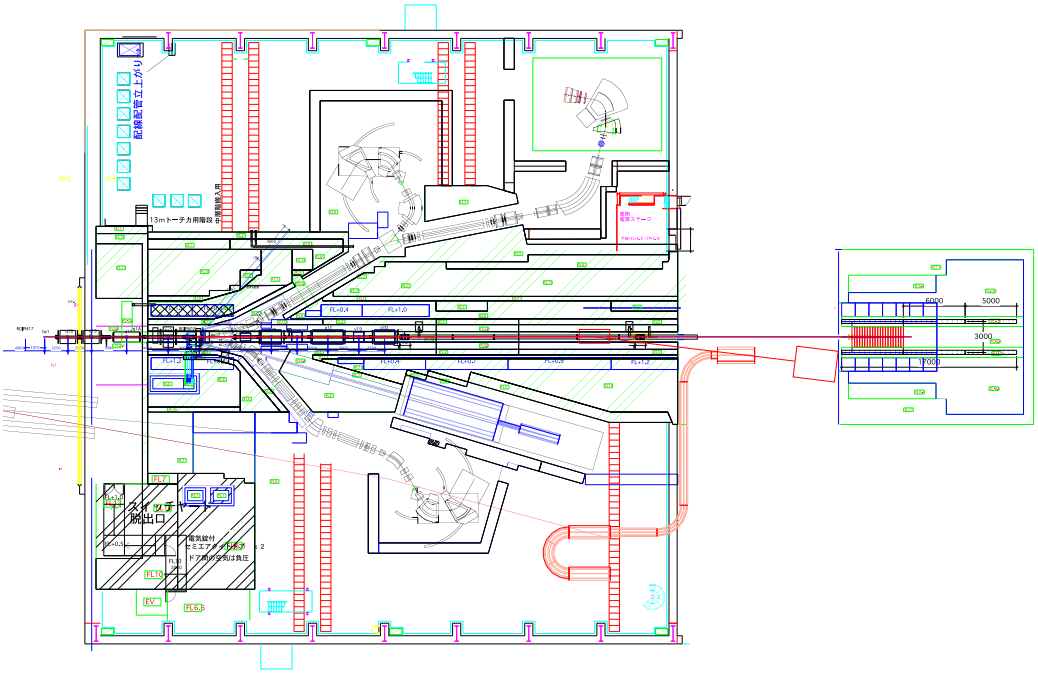

Figure 7.1: A potential layout of the muon beam line and detector using the existing A-Line.

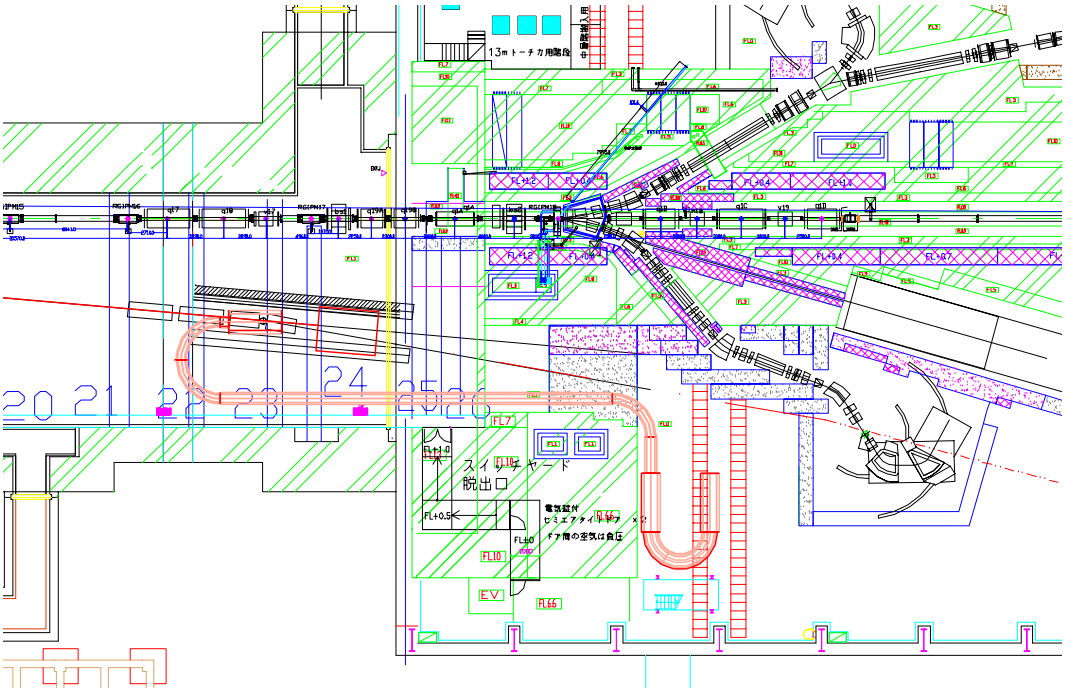

Figure 7.2: A potential layout of the muon beam line and detector using the B-Line. A proton target can be located at the position for the 2nd split.

Chapter 8

Schedule and Cost

8.1 Schedule

The construction of the muon beam line and the detector for the COMET experiment is expected to be complete in 4 years, including one year for the detailed engineering design work and procurement of superconductors and three years for constructions. At the same time, the necessary modification of the proton beam and the experimental hall will have to be made using the budget of the hosting laboratory. We will spend one-year for engineering runs and four-years for physics runs.

Assuming this proposal is optimistically approved in the year of 2008 and the construction is funded quickly, the earliest year to start an engineering run will be around the year of 2013.

8.2 Cost Estimate

A rough cost estimation is made. It does not include any contingencies and infrastructure. It is shown in Table 8.1.

Here, since the detail engineering and design works on the superconducting magnets have not been done, their cost estimation was made using two empirical formulas [47], which are given by

$$\text{cost (M US\$)} = 1.34 \times 0.844 \cdot U^{0.459} \quad (8.1)$$

$$\text{cost (M US\$)} = 1.34 \times 0.77 \cdot \Omega^{0.631}\,, \quad (8.2)$$

where U is a stored energy in an unit of MJ, and Ω is a product of a magnetic field and a volume in an unit of T·m^3. For the superconducting magnets in the proposed experiment, equations (8.1) and (8.2) give 18.0 M US\$ and 20.9 M US\$, respectively. To be conservative, the cost of 20.9 M US\$ is taken. It corresponds to about 2,420 M Japanese Yen (JPY) (when 1 US\$=117 JPY), is taken. In addition, for the B-line scenario, an extension consisting a long superconducting solenoid magnet is needed to accommodate the apparatus in the NP Hall, as was already discussed in Chapter. 7. The extension of the superconductive solenoid would cost about

380 MJPY for about 20 m. It is needless to say that this additional cost strongly depends on the actual layout. It is no doubt that there should exist a large uncertainly in Equations (8.1-8.2). Therefore, a contingency of about 30 % should be considered.

The following items are not included in our cost estimation. They does belong to mostly infrastructures. They are

- modification of an extracted proton beam line and beam monitors,
- a cryogenic system including refrigerators, compressors, a gas buffer tank, and others,
- a proton beam dump,
- a target station and handling system,
- electricity and cooling water systems, and
- radiation shields.

Table 8.1: Rough cost estimation of the COMET experiment. Experimental infrastructure is not included. No contingencies are considered. The uncertainty is relatively large for the moment.

Item	Cost (MJPY)
MR modification[1)]	130
External Extinction Device	230
Production Target & Shield	190
Superconducting Solenoid[2)]	2,420
Pion Capture Solenoid	(870)
Curved Muon Transport Solenoid	(360)
Muon-Stopping Target Solenoid	(530)
Curved Solenoid Spectrometer	(370)
Detector Solenoid	(290)
SC Solenoid Extension (20 m)[3)]	380
Tracking Detector	110
Electron Calorimeter	160
Cosmic Ray Shield	570
Data Acquisition and Trigger	50
Installation and Integration	200
Total	4,440

1) This item may or may not be necessary to achieve the required beam extinction.
2) The breakdown is shown in the following 5 items.
3) This item may or may not be necessary, depending on the layout in the NP Hall.

Chapter 9

Summary

We would like to propose a new experiment (COMET) of searching for coherent neutrino-less $\mu^- - e^-$ conversion in a muonic atom of aluminum, $\mu^- + \mathrm{Al} \rightarrow e^- + \mathrm{Al}$, at a sensitivity of $B(\mu^- \mathrm{Al} \rightarrow e^- \mathrm{Al}) < 10^{-16}$ at J-PARC.

The $\mu^- - e^-$ conversion process is one of the most promising LFV processes to search for. The aimed sensitivity by the proposed experiment is **a factor of 10,000 better** than the present experimental limit. It would offer a wide window and a powerful probe for new physics phenomena beyond the Standard Model, such as supersymmetric grand unification (SUSY-GUT) models and supersymmetric seesaw models with heavy right-handed Majorana neutrinos (SUSY-Seesaw Models) and so on.

To search for a $\mu^- - e^-$ conversion process, **a new innovative muon beam line** with high intensity and high quality, which has not been constructed anywhere in the world, is required. The muon beam line considered in this proposed experiment consists of a section of large solid-angle pion capture by surrounding high-field superconducting solenoid magnets, a section of superconducting curved solenoid magnets for transporting muons and selecting their momenta, and a detector section of curved solenoid spectrometer to detect $\mu^- - e^-$ conversion signals with low counting rate environment. The experiment is planned to be carried out at the J-PARC NP Hall by using a 8-GeV bunched proton beam that is slow-extracted from the J-PARC main ring. The NP hall is only the experimental hall at J-PARC which has a proton beam from slow extraction. And beam bunching is needed to eliminate beam-related background events and keep an experimental sensitivity as high as possible.

This new initiative has been taken to achieve an early and timely start of a series of searches for $\mu^- - e^-$ conversion. We consider that the proposed experiment would have large opportunity for great discovery and J-PARC is the best proton facility to carry out this important experiment.

Bibliography

[1] Kuno Y and Okada Y, 2001 *Rev. of Mod. Phys.* **73** 151

[2] Hincks E P and Pontecorvo B 1947 *Phys. Rev. Lett.* **73** 246

[3] Brooks M L *et al.* (MEGA Collaboration) 1999 *Phys. Rev. Lett.* **83** 1521

[4] Bellgardt U *et al.* 1988 *Nucl. Phys.* B **229** 1

[5] Wintz P 1998 in *Proceedings of the First International Symposium on Lepton and Baryon Number Violation*, edited by H.V. Klapdor-Kleingrothaus and I.V. Krivosheina (Institute of Physics Publishing, Bristol and Philadelphia), p.534. Unpublished.

[6] Burtl W *et al.* (The SINDRUM II Collaboration) 2006 *Eur. Phys. J.* **C 47** 337

[7] Willmann L *et al.* 1999 *Phys. Rev. Lett.* **82** 49

[8] Hayasaka K *et al.* (Belle Collaboration) 2005 *Phys. Lett.* B **613** 20

[9] Abe K *et al.* (Belle Collaboration) 2004 *Phys. Rev. Lett.* **92** 171802

[10] Aubert B *et al.* (BaBar Collaboration) 2004 *Phys. Rev. Lett.* **92** 121801

[11] Krolak P *et al.* 1994 *Phys. Lett.* B **320** 407

[12] Ambrose D *et al.* (BNL E871 Collaboration) 1998 *Phys. Rev. Lett.* **81** 5734

[13] Lee A M *et al.* 1990 *Phys. Rev. Lett.* **64** 165

[14] Arisaka K *et al.* 1998 *Phys. Lett.* B **432** 230

[15] Akers R *et al.* (OPAL Collaboration) 1995 *Z. Phys.* C **67** 555

[16] Abreu P *et al.* (DELPHI Collaboration) 1997 *Z. Phys.* C **73** 243

[17] Hall L J, Kostelecky V A and Raby S 1986 *Nuclear Physics* B **267** 415

[18] Barbieri R, Hall L and Strumia A 1995 *Nuclear Physics* B **445** 219

[19] Hisano J, Moroi T, Tobe K, and Yamaguchi M 1997 *Phys. Lett.* B **391** 341; Erratum 1997 *Physics Letters* B **397** 357

[20] Hisano J, Moroi T, Tobe T, Yamaguchi M, and Yanagida T 1995 *Phys. Lett.* B **357** 576

[21] Hisano J, Nomura D, and Yanagida T 1998 *Physics Letters* B **437** 351

[22] Hisano J and Nomura D 1999 *Phys. Rev.* D **59** 116005

[23] Tobe Wells J D, and Yanagida T 2004 *Phys. Rev.* D **69** 035010

[24] Masiero A, Profumo S, Vempoti S K, and Yaguna C E 2004 *JHEP* 0403:046

[25] Shanker O 1982 *Phys. Rev.* D **25** 1847

[26] Watanabe R, Fukui M, Ohtsubo H and Morita M, 1987 *Prog. Theor. Phys.* **78** 114; Watanabe R, Muto K, Oda T, Niwa T, Ohtsubo H, Morita R and Morita M, 1993 *At. Data Nucl. Data Tables* **54** 165

[27] Bryman D A, Blecher M, Gotow K and Powers R J 1972 *Phys. Rev. Lett.* **28** 1469

[28] Badertscher A *et al.* 1982 *Nucl. Phys.* A **377** 406

[29] Bryman D A *et al.* 1985 *Phys. Rev. Lett.* **55** 465

[30] Ahmad S *et al.* 1988 *Phys. Rev.* D **38** 2102

[31] Dohmen C *et al.* (SINDRUM II Collaboration) 1993 *Phys. Lett.* B **317** 631

[32] Honecker W *et al.* (SINDRUM II Collaboration) 1996 *Phys. Rev. Lett.* **76** 200 *Eur. Phys. J. C* **47**, 337.

[33] Bachman M *et al.* 1997, a research proposal to Brookhaven National Laboratory AGS "A Search for $\mu^- N \to e^- N$ with Sensitivity Below 10^{-16}, **M**uon – **E**lectron **CO**nversion"

[34] Barkov L M *et al.* 1999, a research proposal to PSI "Search for $\mu^+ \to e^+\gamma$ down to 10^{-14} branching ratio"

[35] A Letter of Intent to the J-PARC 50 GeV Proton Synchrotron Experiments, "The PRISM Project - A Muon Source o the World-Highest Brightness by Phase Rotation -", January 1st, 2003

[36] A Letter of Intent to the J-PARC 50 GeV Proton Synchrotron Experiments, "An Experimental Search for the $\mu^- - e^-$ Conversion Process At An Ultimate Sensitivity Of The Order of 10^{-18} With PRISM", January 1st, 2003

[37] A Letter of Intent to the J-PARC 50 GeV Proton Synchrotron Experiments, "An Experimental Search for a $\mu^- - e^-$ Conversion at Sensitivity of the Order of 10^{-18} With A Highly Intense Muon Source, PRISM". April 28th, 2006.

[38] MECO Technical Proposal, August 1, 2001, unpublished.

[39] A Letter of Intent on "A Muon to Electron Conversion Experiment at Fermilab", The Mu2e Collaboration, 2007

[40] MECO Superconducting Solenoid System Conceptual Design Report, June 6, 2002, unpublished.

[41] *http://g4beamline.muonsinc.com*

[42] Hänggi P, Viollier R D, Raff U nd Adler K 1974 *Phys. Lett.* B **51** 119

[43] Herzog F and Adler K 1980 *Helv. Phys. Acta* **53** 53

[44] Kozlowski T *et al.*, 1985 *Nucl. Phys.* A **436** 717

[45] Wyttenbach A *et al.*, 1978 *Nucl. Phys.* A **294** 278

[46] Krane K S *et al.*, 1979 *Phys. Rev.* C **20** 1873

[47] Palmer R B and Berg J S, 2004 in *Proceedings of EPAC 2004*, Lucerne, Switzerland p.1807.